Stem Cell Reports
Article
OPEN ACCESS

Human Induced Pluripotent Stem Cell-Derived Cardiac Cell Sheets Expressing Genetically Encoded Voltage Indicator for Pharmacological and Arrhythmia Studies

Naim Shaheen,[1,3] Assad Shiti,[1,3] Irit Huber,[1] Rami Shinnawi,[1] Gil Arbel,[1] Amira Gepstein,[1] Noga Setter,[1] Idit Goldfracht,[1] Amit Gruber,[1] Snizhanna V. Chorna,[1] and Lior Gepstein[1,2,*]
[1]Sohnis Research Laboratory for Cardiac Electrophysiology and Regenerative Medicine, The Rappaport Faculty of Medicine and Research Institute, Technion - Israel Institute of Technology, Haifa, Israel, POB 9649, Haifa 3109601, Israel
[2]Cardiolology Department, Rambam Health Care Campus, Haliya Hashniya St 8, Haifa 3109601, Israel
[3]Co-first author
*Correspondence: mdlior@technion.ac.il
https://doi.org/10.1016/j.stemcr.2018.04.006

SUMMARY

Fulfilling the potential of human induced pluripotent stem cell (hiPSC)-derived cardiomyocytes for studying conduction and arrhythmogenesis requires development of multicellular models and methods for long-term repeated tissue phenotyping. We generated confluent hiPSC-derived cardiac cell sheets (hiPSC-CCSs), expressing the genetically encoded voltage indicator ArcLight. ArcLight-based optical mapping allowed generation of activation and action-potential duration (APD) maps, which were validated by mapping the same hiPSC-CCSs with the voltage-sensitive dye, Di-4-ANBDQBS. ArcLight mapping allowed long-term assessment of electrical remodeling in the hiPSC-CCSs and evaluation of drug-induced conduction slowing (carbenoxolone, lidocaine, and quinidine) and APD prolongation (quinidine and dofetilide). The latter studies also enabled step-by-step depiction of drug-induced arrhythmogenesis ("torsades de pointes in the culture dish") and its prevention by $MgSO_4$ and rapid pacing. Phase-mapping analysis allowed biophysical characterization of spiral waves induced in the hiPSC-CCSs and their termination by electrical cardioversion and overdrive pacing. In conclusion, ArcLight mapping of hiPSC-CCSs provides a powerful tool for drug testing and arrhythmia investigation.

INTRODUCTION

The introduction of the human induced pluripotent stem cell (hiPSC) technology (Takahashi et al., 2007) coupled with improved methods for cardiomyocyte differentiation (Burridge et al., 2014; Mummery et al., 2012) brought a unique value to the fields of cardiac disease modeling (Bellin and Mummery, 2016; Itzhaki et al., 2011; Matsa et al., 2016; Moretti et al., 2010; Shaheen et al., 2017; Sun et al., 2012) and drug testing (Liang et al., 2013; Shinnawi et al., 2015; Stillitano et al., 2017; Zwi et al., 2009). In the field of cardiac electrophysiology, most studies examined the electrical properties of the hiPSC-derived cardiomyocytes (hiPSC-CMs) at the single-cell level, focusing primarily on action potential (AP) and ionic current characteristics. Only a few studies have utilized multicellular hiPSC-based cardiac tissue models to evaluate conduction and arrhythmogenesis (Herron, 2016; Kadota et al., 2013; Laksman et al., 2017; Lee et al., 2012).

Traditional methodologies used for studying conduction in cardiomyocyte cultures include multielectrode extracellular recordings (Yankelson et al., 2008), which may be limited in terms of spatial resolution and degree of complexity of the information gained, or optical mapping (Herron et al., 2012). The latter approach utilizes voltage-sensitive dyes (VSDs) to follow changes in membrane potential (Lopez-Izquierdo et al., 2014; Matiukas et al., 2007). These indicators, although of great utility, can cause phototoxicity and hamper the ability to obtain long-term and repeated recordings.

To overcome the aforementioned challenges, we propose to combine the hiPSC technology, two-dimensional (2D) cardiac tissue models, and genetically encoded voltage indicators (GEVIs), such as ArcLight (Leyton-Mange et al., 2014; Shinnawi et al., 2015), VSFP-CR (Chen et al., 2017), CaViar (Dempsey et al., 2016), and VSFP2.3 (Liao et al., 2015), for probing membrane potentials. Specifically, we chose to focus on ArcLight and hypothesized that the generated ArcLight-expressing hiPSC-derived cardiac cell sheets (hiPSC-CCSs) will allow gaining high-resolution information regarding tissue conduction and repolarization in both acute and long-term studies. Following establishment of this unique multicellular model, we aimed to evaluate its potential for drug testing using agents known to alter conduction and/or repolarization with specific emphasis on studying the mechanisms of drug-induced arrhythmias at the tissue level. Finally, we aimed to evaluate the biophysical properties of reentrant arrhythmias (spiral waves) induced in this model through either a drug-related pro-arrhythmia mechanism or following programmed electrical stimulation and to test the efficacy of clinically relevant therapeutic interventions.

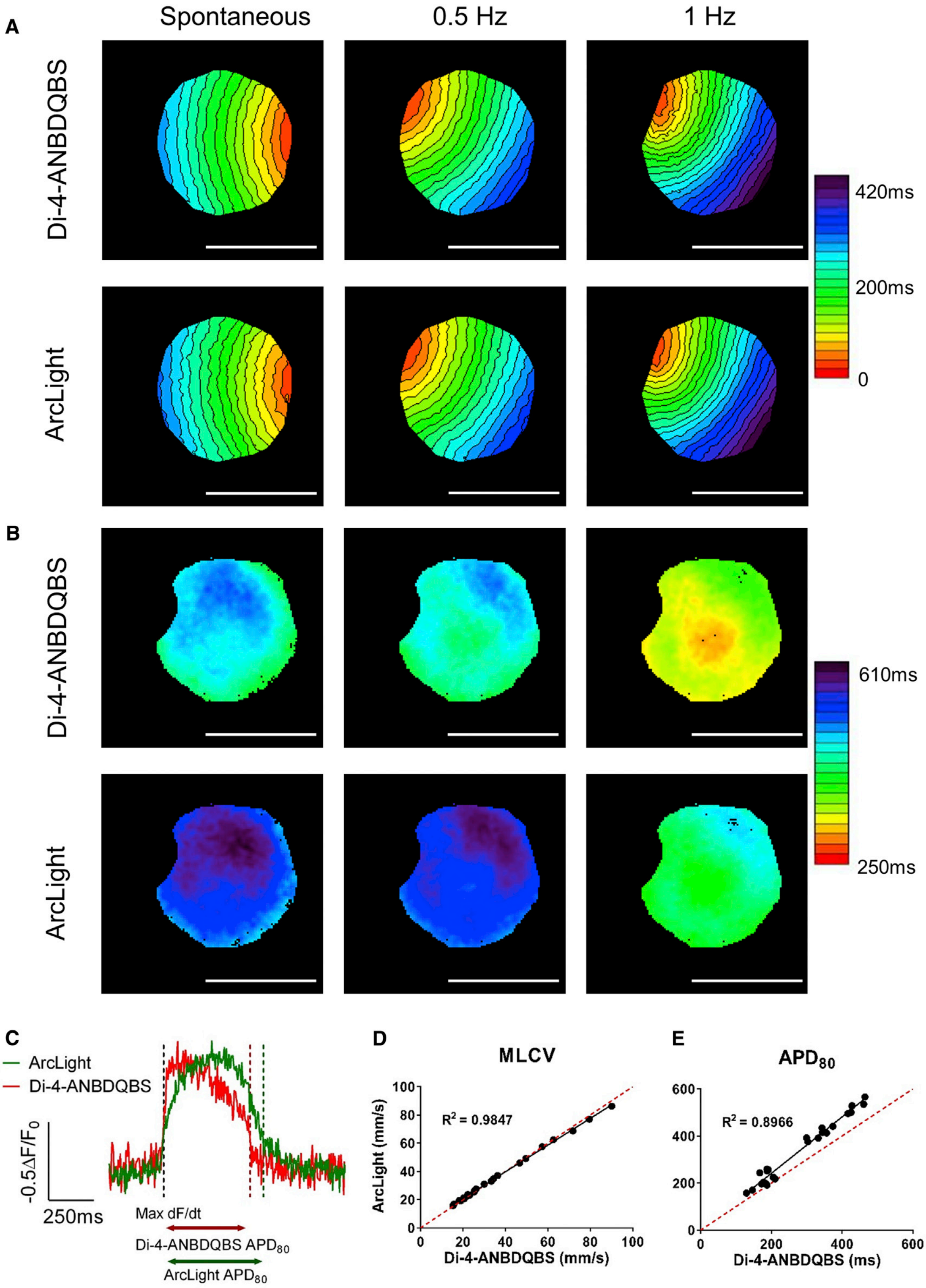

Figure 1. ArcLight versus Di-4-ANBDQBS: Mapping Comparison

(A and B) Activation (A) and APD_{80} (B) maps of the same ArcLight-hiPSC-CCS generated from analysis of Di-4-ANBDQBS (top) and ArcLight (bottom) signals during spontaneous activity, 0.5 Hz and 1 Hz pacing frequencies. Single isochrone: 20 ms. Scale bars: 5 mm.

(legend continued on next page)

RESULTS

Generation of ArcLight-Expressing hiPSC-CCSs

ArcLight-expressing hiPSCs from a stable transgenic line established in our laboratory (Shinnawi et al., 2015) were differentiated into the cardiac lineage using a modified directed small-molecule monolayer-based differentiation system (Burridge et al., 2014). Following differentiation, beating monolayers, containing ≥85% cardiomyocytes (Figure S1A), were enzymatically dissociated and seeded as circular homogeneous hiPSC-CCSs (Figure S1B).

A series of experimental calibration and optimization steps were then performed to determine the optimal seeding density required to obtain hiPSC-CCSs, which will be highly confluent but without evidence for cell death due to improper diffusion. The optimal approach, according to these studies, consisted of using only highly enriched early-stage differentiated cardiomyocytes (>85% cardiac troponin T positive, 8–14 days post differentiation). Tissues were generated from single-cell suspensions, derived following enzymatic dissociation and the use of a 100 μm cell strainer, at a seeding density of 38,000–56,000 cells/mm^2. We chose to generate hiPSC-CCSs with a ~0.5 cm diameter, as this size was sufficient for monitoring electrical propagation, measuring local conduction velocities (CVs), and inducing arrhythmias.

We next performed cell content analysis by enzymatically digesting hiPSC-CCSs at different developmental stages. This time-series analysis (Figure S1C) revealed a major drop in cell content between day 0 (d0) and d1, and a relatively stable cell content after d6–10. The final cell count was ~400,000 cells/hiPSC-CCS, which was sufficient to achieve homogeneous tissues without any structural discontinuities in 80%–90% of independent sessions.

Immunostaining of sarcomeric α-actinin and connexin 43 (Cx43) confirmed the presence of high-density electrically coupled cardiomyocytes arranged in an isotropic pattern within the hiPSC-CCSs (Figure S1). Structural characterization using three-dimensional reconstruction (Figures S1D–S1F) and orthogonal views (Figure S2G) revealed that the final tissues consisted of approximately four cell layers (range, 3–7; n = 13 from four independent experiments) with a thickness of 19.1 ± 8.4 μm.

Comparison of ArcLight and Di-4-ANBDQBS-Based Optical Mapping

We hypothesized that GEVIs can be utilized for long-term and repeated electrophysiological phenotyping without affecting cell viability. The ability of ArcLight to evaluate human cardiomyocyte AP morphology and duration was already demonstrated at the cellular level (Leyton-Mange et al., 2014; Shinnawi et al., 2015) but has not been utilized at the tissue level to evaluate conduction. One potential limitation of GEVIs in general and ArcLight specifically is their relatively slow kinetics (Jin et al., 2012), a property that may hinder their potential use for activation mapping. To evaluate whether, despite this limitation, ArcLight imaging can still be used to reliably evaluate tissue conduction, we compared the results of ArcLight-based activation mapping with similar maps obtained using conventional VSD-based mapping over a wide array of conditions (Figures 1 and S2–S4).

ArcLight-hiPSC-CCSs (6–35 days post plating) were loaded with the VSD, Di-4-ANBDQBS, paced at variable cycle lengths (CLs, 300–2,000 ms) and alternatingly imaged by manual interchanging between two filter sets, one for obtaining ArcLight optical signals and the other for Di-4-ANBDQBS signals (Figure S2A). These studies verified the development of a functional syncytium, enabled monitoring of AP wave propagation (Video S1), and allowed construction of detailed activation and APD maps using both ArcLight and Di-4-ANBDQBS signals (Figures 1, S2, and S3).

We found that the slower kinetics of ArcLight affected mostly the final portion of phase 0 of the AP (Figures 1C and S2E). Consequentially, by defining the local activation time (LAT) as the time point of the maximum first derivative of the recorded signal at each pixel (Figures 1C and S2E), we were able to construct ArcLight-based activation maps that did not differ from those generated using Di-4-ANBDQBS mapping (Figures 1A, S2, and S3). This was also confirmed quantitatively, as a high correlation (R^2 = 0.985, Figure 1D, n = 25) was found between the mean local conduction velocities (MLCV) measured from the corresponding ArcLight and Di-4-ANBDQBS maps across a wide range of MLCV values. The agreement between ArcLight and Di-4-ANBDQBS mapping was also validated when using different signal-acquisition rates (260 and 520 frames/s, Figures S3A–S3C). Similarly, the average APD_{80} (APD at 80% repolarization) values measured by

(C) Representative traces of Di-4-ANBDQBS (red) and ArcLight (green) optical APs recorded from the same region of interest (ROI) (3 × 3 pixels).

(D) Correlation between MLCVs values, as derived from ArcLight and Di-4-ANBDQBS activation maps in the same cultures. Notice the high correlation (R^2 = 0.9847, n = 25 from four independent experiments) in MLCVs measurements made by the two methods.

(E) Similar comparison of the mean APD_{80} as measured from ArcLight and Di-4-ANBDQBS recordings (R^2 = 0.8966, n = 25 from four independent experiments).

See also Figures S1–S4 and Video S1.

ArcLight correlated ($R^2 = 0.897$, Figure 1E, n = 25) with the measurements derived from Di-4-ANBDQBS recordings over a wide range of values. Notice that, despite this high correlation, ArcLight APD_{80} values tended to overestimate APD as compared with Di-4-ANBDQBS recordings (Figures 1B and 1E).

ArcLight Displays Decreased Phototoxicity

We next attempted to compare ArcLight- with VSD-based mapping in regards to signal-to-noise ratio (SNR) and phototoxicity. In a series of preliminary studies, we found that the optimal loading conditions of Di-4-ANBDQBS were 60 μg/mL for 20 min. Using these conditions, we noted that the SNR values of Di-4-ANBDQBS were comparable with that of ArcLight ($p > 0.05$, n = 9, Figure S4A). This finding was verified using additional four different formulas previously utilized to calculate SNR (data not shown).

In order to compare the potential cytotoxic effects of both indicators, we illuminated a focused area within the ArcLight-hiPSC-CCSs for 10 min (central portion in Figure S4B). These studies were conducted in ArcLight-hiPSC-CCSs that were also loaded with Di-4-ANBDQBS and compared with hiPSC-CCSs expressing ArcLight alone or Di-4-ANBDQBS alone (Figure S4C). ArcLight-hiPSC-CCSs were also exposed to red illumination to rule out the contribution of this factor. Our results show a significant decline in the optical signals in the two groups containing Di-4-ANBDQBS ("ArcLight + Di-4-ANBDQBS" and "Di-4-ANBDQBS alone"; Figure S4C). Importantly, the decline in optical signal in the ArcLight + Di-4-ANBDQBS group was not restricted to Di-4-ANBDQBS signal but was also present in ArcLight recordings (Figure S4C). In contrast, the decline in the optical signal was minimal in the "ArcLight alone" hiPSC-CCSs groups exposed to either blue or red illumination (Figure S4C).

The aforementioned results suggest a potential phototoxic effect induced by Di-4-ANBDQBS. To test this hypothesis, we illuminated only the central portion of hiPSC-CCSs (Figure S4B) for 20 min and then labeled the tissues with DAPI. We then quantified the DAPI signal (as a marker of membrane damage or cell death) in the central illuminated area and normalized it by the DAPI signal in the non-illuminated peripheral area (center/periphery DAPI ratio). As shown in Figures S4C and S4D, an increased toxicity at the illuminated center was only observed in the two groups loaded with Di-4-ANBDQBS (ArcLight + Di-4-ANBDQBS and Di-4-ANBDQBS alone) and was lacking in the blue or red-illuminated ArcLight alone group and in the control hiPSC-CCS group (lacking both reporters) (Figures S4C and S4D). These results suggest that ArcLight-based imaging may be less cytotoxic and therefore more suitable for long-term and repeated tissue phenotyping.

Repeated Long-Term Analysis of the ArcLight-hiPSC-CCSs

To test the hypothesis that ArcLight-based optical mapping can allow repeated and long-term analysis, we followed the electrical remodeling process of the ArcLight-hiPSC-CCSs for more than a month. Figures 2A and 2B depict changes in mean APD_{80} and MLCV values respectively, at each time point, for the seven cultures studied while paced at 1 Hz. These long-term studies revealed gradual shortening of mean APD values (Figure 2A, $p < 0.0001$, n = 7) and a gradual increase in CV values (Figure 2B), with the fastest CVs peaking at d16–20 ($p < 0.0001$, n = 7) and then slightly declining ($p > 0.05$) at d26–35.

To address the mechanisms underlying the CV changes over time, we focused on Cx43 expression (as a surrogate for intercellular coupling) and on Na^+ current recordings (as a surrogate for membrane excitability). As shown in the western blot analysis in Figures S5A and S5B, we did not observe any consistent changes in Cx43 expression between hiPSC-CCSs at 6–10 days versus 16–20 days. Next, we conducted voltage-clamp studies to measure I_{Na+} from single dispersed hiPSC-CMs, derived from hiPSC-CCSs at 6 days or 20 days post plating. As depicted in the current-voltage curves in Figure S5C, cardiomyocytes derived from hiPSC-CCSs at d20 displayed significantly higher peak-current densities (106.5 ± 13.2 versus 70.1 ± 9.9 pA/pF, $p < 0.01$, n = 15 and 13).

Finally, we aimed to test the suitability of ArcLight-hiPSC-CCSs for repeated pharmacological studies by conducting multiple recordings from the same culture over several days and applying different repolarization-altering drugs at each day (10 nmol/L dofetilide and 5 μmol/L quinidine). The results demonstrate APD_{80} prolongation in response to each compound followed by recovery to baseline values following drug washout (Figure 2C).

Pharmacological and Pacing Studies

We next aimed to monitor the effects of different interventions on the electrophysiological properties of the hiPSC-CCSs. We first tested the effects of altering pacing frequency (1, 1.25, 1.67, 2 Hz) on the tissues' AP (APD) and conduction (MLCV) properties. Notice in the resulting restitution plots (Figure 2D) the expected APD shortening ($p < 0.01$, n = 6) and CV slowing ($p < 0.0001$, n = 7) with higher pacing frequencies.

We next tested the effects of different drugs on the electrical properties of the hiPSC-CCSs. The drugs tested included agents known to slow conduction via two different mechanisms: (1) carbenoxolone (50 μmol/L), a gap-junction blocker; and (2) lidocaine (1–300 μmol/L), a class Ib antiarrhythmic agent that blocks the fast voltage-gated Na^+ channels. Both agents (n = 5) significantly

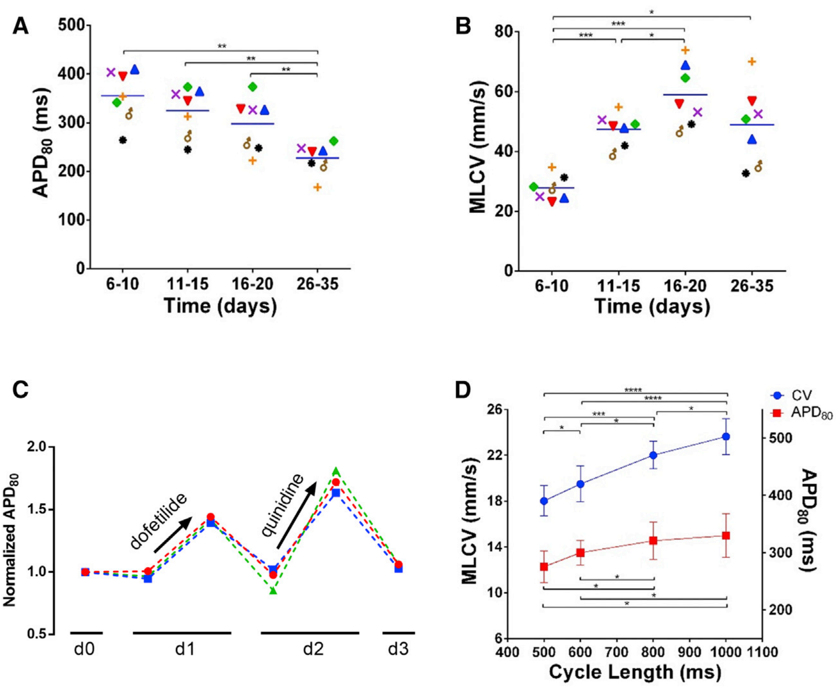

Figure 2. Effects of Culture Time, Pacing Frequency, and Repeated Drug Applications on APD$_{80}$ and CV Measurements

(A and B) Summary of mean APD$_{80}$ (A) and MLCV (B) values as a function of culture time in ArcLight-hiPSC-CCSs (repeated-measurements one-way ANOVA followed by Tukey post-hoc analysis, n = 7 from three independent experiments).

(C) Summary of changes in the normalized APD$_{80}$ values over time in three hiPSC-CCSs during repeated drug experiments (dofetilide and quinidine).

(D) Restitution curves summarizing the changes in MLCV and mean APD$_{80}$ values in hiPSC-CCS (6–10 days post plating) as function of pacing cycle length (repeated-measurements one-way ANOVA followed by Tukey post-hoc analysis, n = 7 and 6 respectively, from three independent experiments).

Values are presented as means ± SEM. $^*p < 0.05$, $^{**}p < 0.01$, $^{***}p < 0.001$, and $^{****}p < 0.0001$. See also Figures S3 and S5.

slowed conduction in all cultures, as depicted in the activation maps presented prior to and after drug application (Figure 3A, left panels). Note also the typical dose-response effect of lidocaine on MLCV (Figure 3A, middle-right panels).

We next tested the ability to detect repolarization changes by applying dofetilide (0.3–100 nmol/L), a class III antiarrhythmic agent that blocks I_{Kr}. As expected, dofetilide led to significant APD prolongation, as depicted in the APD$_{80}$ map example (Figure 3B, top-left panels) and in the plot summarizing the dose-response changes in mean APD$_{80}$ for all cultures (Figure 3B, top-right panel; n = 5).

Finally, we tested the effects of quinidine (0.1–30 μmol/L), a Na^+ channel blocker with additional nonspecific potassium channels blocking activity. The resulting activation (Figure 3A, bottom-left panels) and APD$_{80}$ (Figure 3B, bottom-left panels) maps and the corresponding dose-response curves (bottom-right panels, n = 5) revealed the dual effect of quinidine, both slowing conduction and prolonging APD in the hiPSC-CCSs.

Modeling Reentrant Arrhythmia (Spiral Waves)

We next aimed to evaluate whether ArcLight imaging could go beyond assessment of conduction in the hiPSC-CCSs and also be used to detect, monitor, and study reentrant arrhythmias. To this end, we aimed to induce arrhythmias in the hiPSC-CCSs through a systematic electrical stimulation approach: starting by an increase in stimulation frequency followed by burst pacing and finally direct current injection (Video S2). Using this induction protocol, we were able to induce reentrant arrhythmias in 30% of the hiPSC-CCSs and to monitor the resulting rotors' activities using ArcLight optical signals. Once initiated, the rotors (spiral waves) were highly stable and were associated with a significant increase ($p < 0.05$) in the frequency of activation (CL = 476 ± 237 ms) as compared with baseline spontaneous activity (CL = 2,853 ± 1,114 ms, n = 5).

The propagation of the spiral waves could be followed by ArcLight optical mapping, either as dynamic displays depicting the changes in ArcLight fluorescence (Video S3, upper panels) or by constructing detailed activation maps (Figure 4A). An alternative strategy to characterize complex reentrant activity is phase mapping (Gray et al., 1998; Hou et al., 2010; Iyer and Gray, 2001; Pandit and Jalife, 2013). The constructed phase maps, generated by mathematical processing of the optical signals, could be used to characterize the spiral waves either as snapshots (Figure 4B) or as dynamic displays (Video S3, lower-panels). This approach makes it possible to follow the propagation of the rotor's wave front, its singularity point (SP) (the point where all phases conjoin, depicted as black dots in Figure 4B and Video S3), and its meandering path (Figure 4C). Such analysis also allows quantification of various spiral wave biophysical properties, including the rotor's frequency (2.53 ± 1.14 Hz, n = 5, Figure 4D), radius (inversely proportional to curvature, 2.59 ± 1.48 mm; Figure 4D), and the

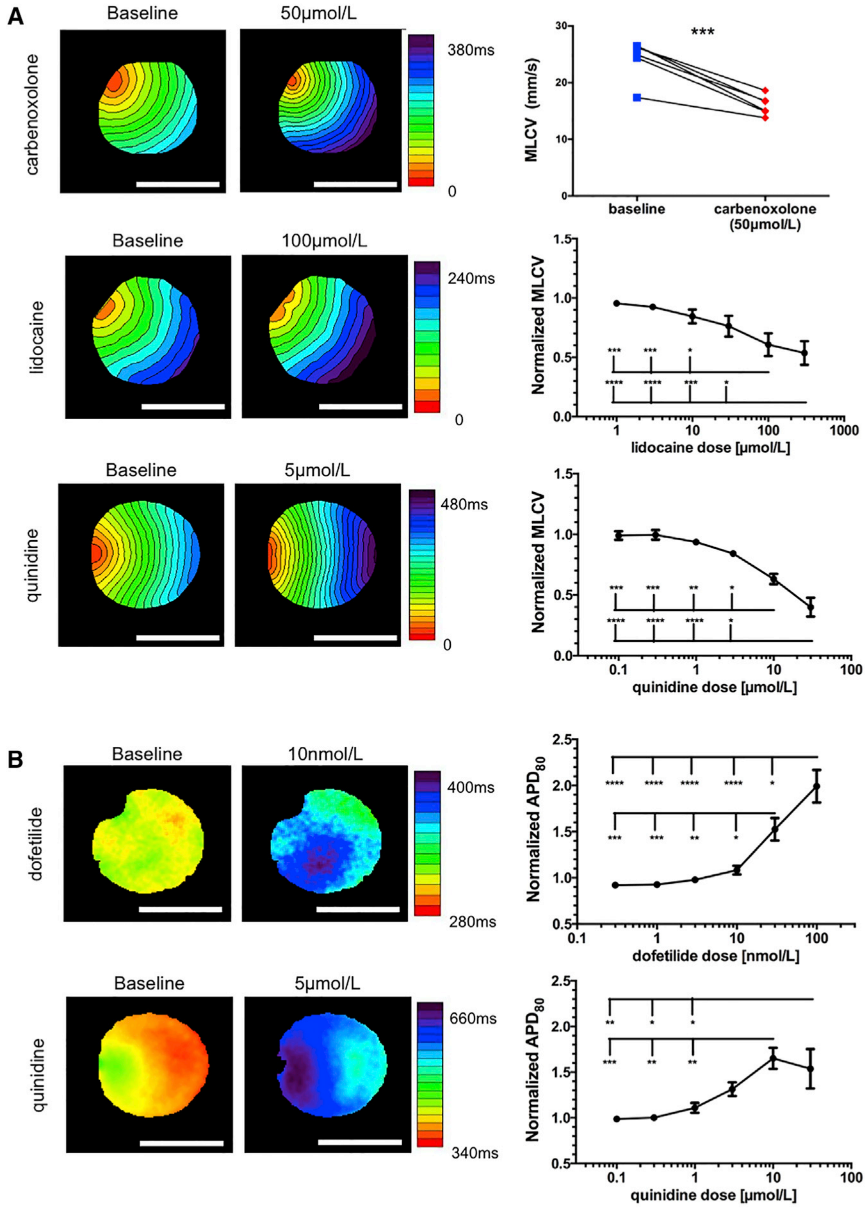

Figure 3. Pharmacological Effects on Repolarization and Conduction

(A) Representative activation maps (left and middle) and dose-response curves (right) of CV slowing drugs: carbenoxolone (50 μmol/L, n = 5 from three independent experiments, paired t test), lidocaine (1, 3, 10, 30, 100, and 300 μmol/L), and quinidine (0.1, 0.3, 1, 3, 10, and 30 μmol/L). Multiple comparisons were made using one-way ANOVA followed by Tukey post-hoc analysis, both n = 5 from four and three independent experiments, respectively.

(B) Representative APD$_{80}$ maps (left and middle) and dose-response curves (right) of APD prolonging drugs: dofetilide (0.3, 1, 3, 10, 30, and 100 nmol/L) and quinidine (0.1, 0.3, 1, 3, 10, and 30 μmol/L). Multiple comparisons made using one-way ANOVA followed by Tukey post-hoc analysis, both n = 5 from three independent experiments). Scale bars: 5 mm. Values are presented as means ± SEM. $^*p < 0.05$, $^{**}p < 0.01$, $^{***}p < 0.001$ and $^{****}p < 0.0001$. See also Figure S3.

spatial quantification of SP meandering (1.34 ± 1.50 mm; Figures 4C and 4D).

We next evaluated whether clinically relevant maneuverers such as electrical cardioversion and overdrive pacing can terminate such reentrant arrhythmias. To allow field electrical cardioversion, we placed bipolar electrodes at opposing borders of the hiPSC-CCSs (Figure S2D) and applied a 50 ms biphasic pulse over the entire tissue. This resulted in arrhythmia termination in seven out of seven cultures studied, as shown in Figures 5A–5C and Video S4.

As for overdrive pacing, we performed point stimulation of the hiPSC-CCSs at rates faster than arrhythmia's CL, as shown in Figures 5D–5I and Video S5. Figures 5D and 5E show the fluorescent signals recorded from two sites in a hiPSC-CCS with stable rotor activity (phase map in Figure 5F) with a CL of 350 ms. Next, the electrical wave initiated by the high-frequency pacing (CL = 300 ms) was able to drive the reentrant activity to the top edge of the hiPSC-CCS (Figure 5G, note the black trace and white arrow showing the migration path of the rotor's SP). Occasionally, as shown in this example, new rotors emerged during overdrive pacing, which were also driven to the edge of the culture (Figure 5H), leading eventually to arrhythmia termination and restoration of normal activity (Figure 5I). Figure 5J summarizes the cumulative cardioversion rate in

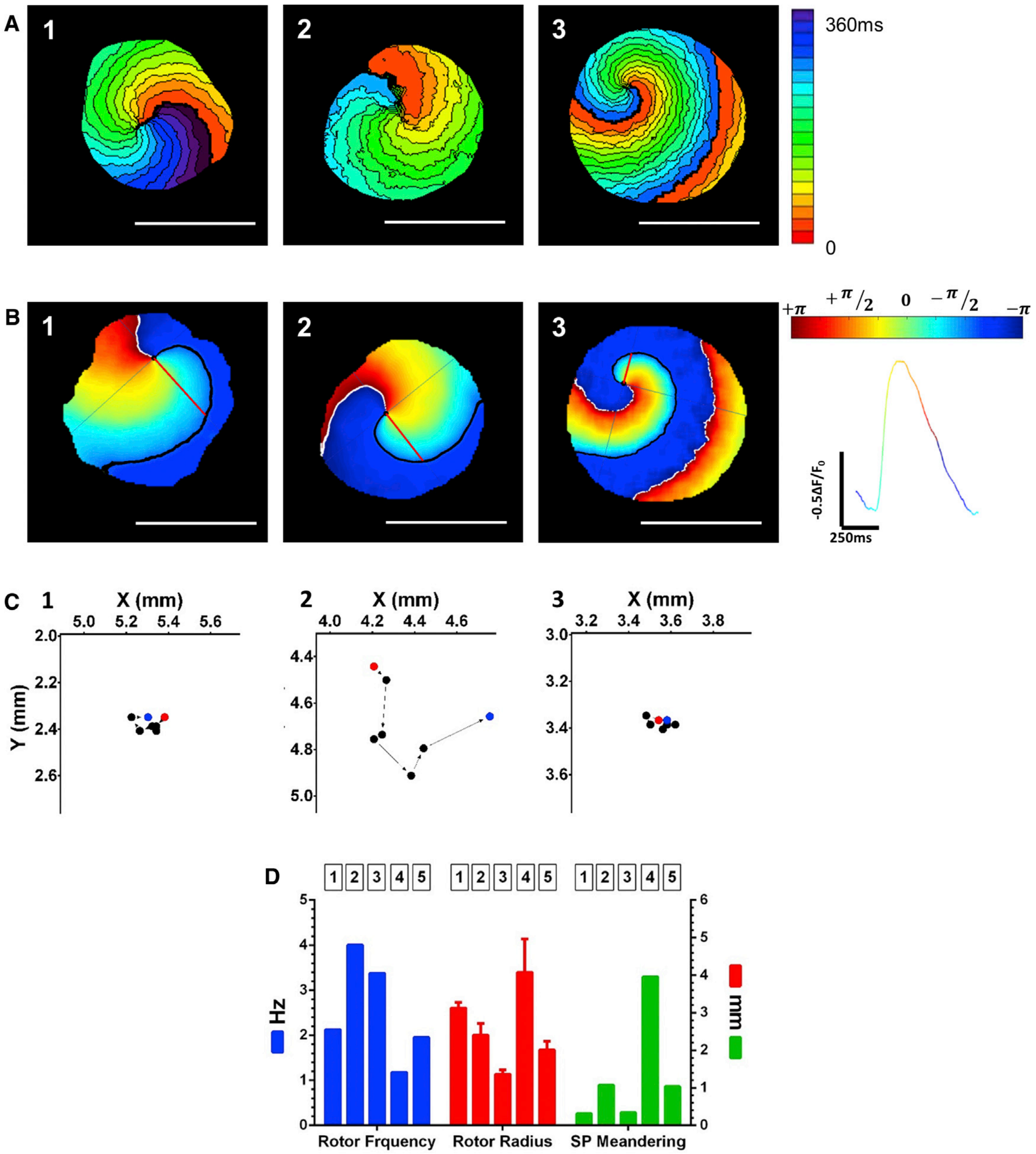

Figure 4. Analysis of Spiral Waves (Rotors)

(A) Activation maps of the induced rotors in three ArcLight-hiPSC-CCSs. Single isochrones: 20 ms.

(B) Snapshots of phase maps of the same rotors. Colors represent phase, as in the color bar and the colored signal (right). Singularity points (SPs) are indicated as black dots. Black and white lines indicate the wave fronts and tails respectively. Red lines extending from the SP to the wave front, indicate radiuses of the curvatures.

(C) Trajectory of SP meandering for each of the three rotors; total pathway of six SP steps over one rotation cycle.

(D) Summary of rotating frequency (2.526 ± 1.141 Hz), rotor radius (2.594 ± 1.48 mm; error bars represent SEM), and SP meandering pathway (1.342 ± 1.505 mm) of five rotors (from three independent experiments).

Scale bars: 5 mm. See also Figure S2 and Videos S2 and S3.

all hiPSC-CCSs studied following sequential increases in pacing frequency (defined as "rotor CL-pacing CL"), leading to termination of reentrant activity in six out of seven cultures studied.

Drug-Induced Pro-arrhythmia (Torsades de Pointes in the Dish)

Recent studies demonstrated the potential of hiPSC-CMs in the field of safety pharmacology by detecting drug-induced

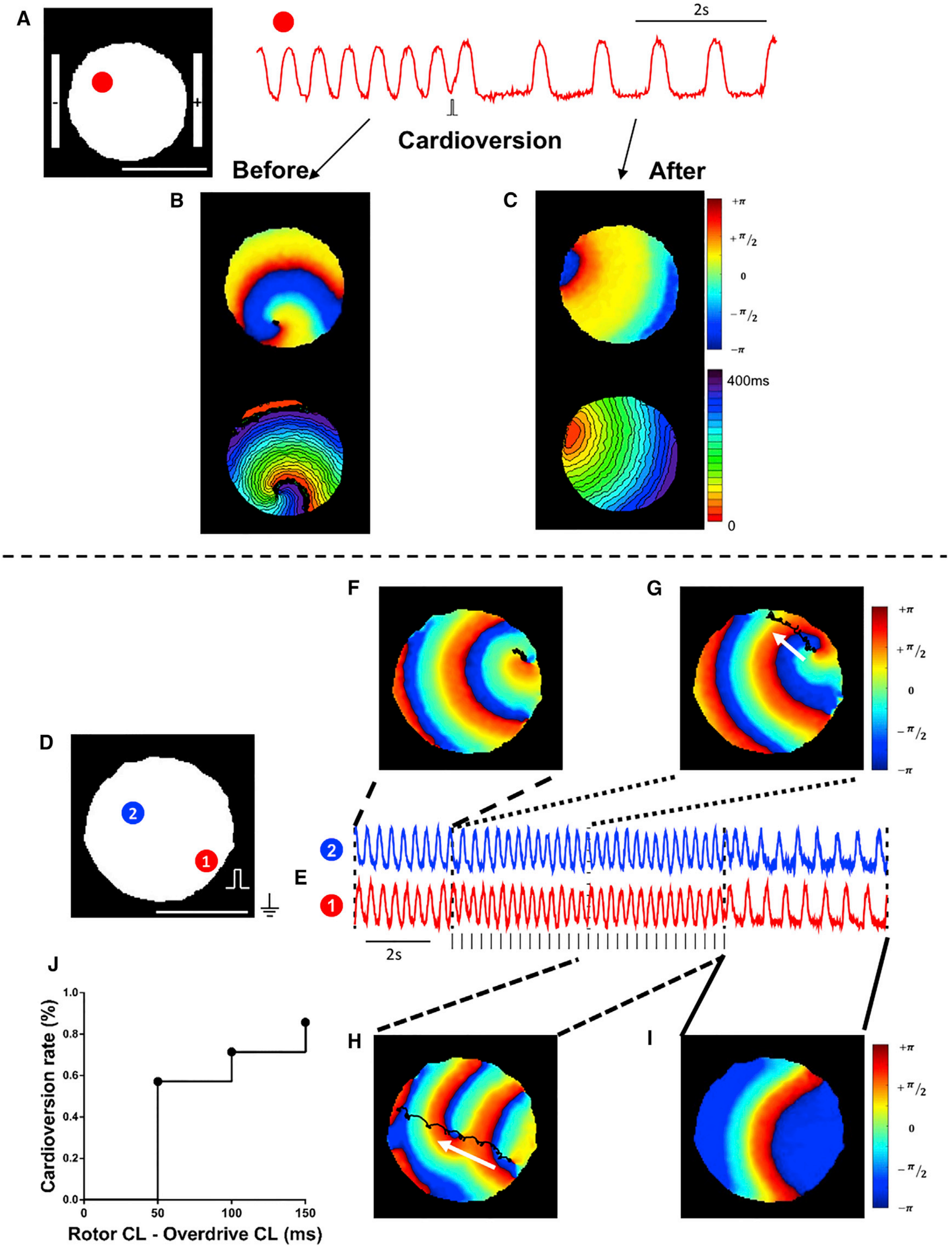

Figure 5. Spiral Waves Termination by Electrical Cardioversion and Overdrive Pacing
(A) Fluorescent trace from one area (red) in an ArcLight-hiPSC-CCS exhibiting stable spiral wave.
(B and C) Phase (upper panel) and activation (lower panel) maps before (B) and after (C) electric cardioversion.
(D and E) Fluorescence traces from two points, 1 (red) and 2 (blue), in an ArcLight-hiPSC-CCS exhibiting stable spiral wave. Vertical marks denote timing of pacing pulses.

(legend continued on next page)

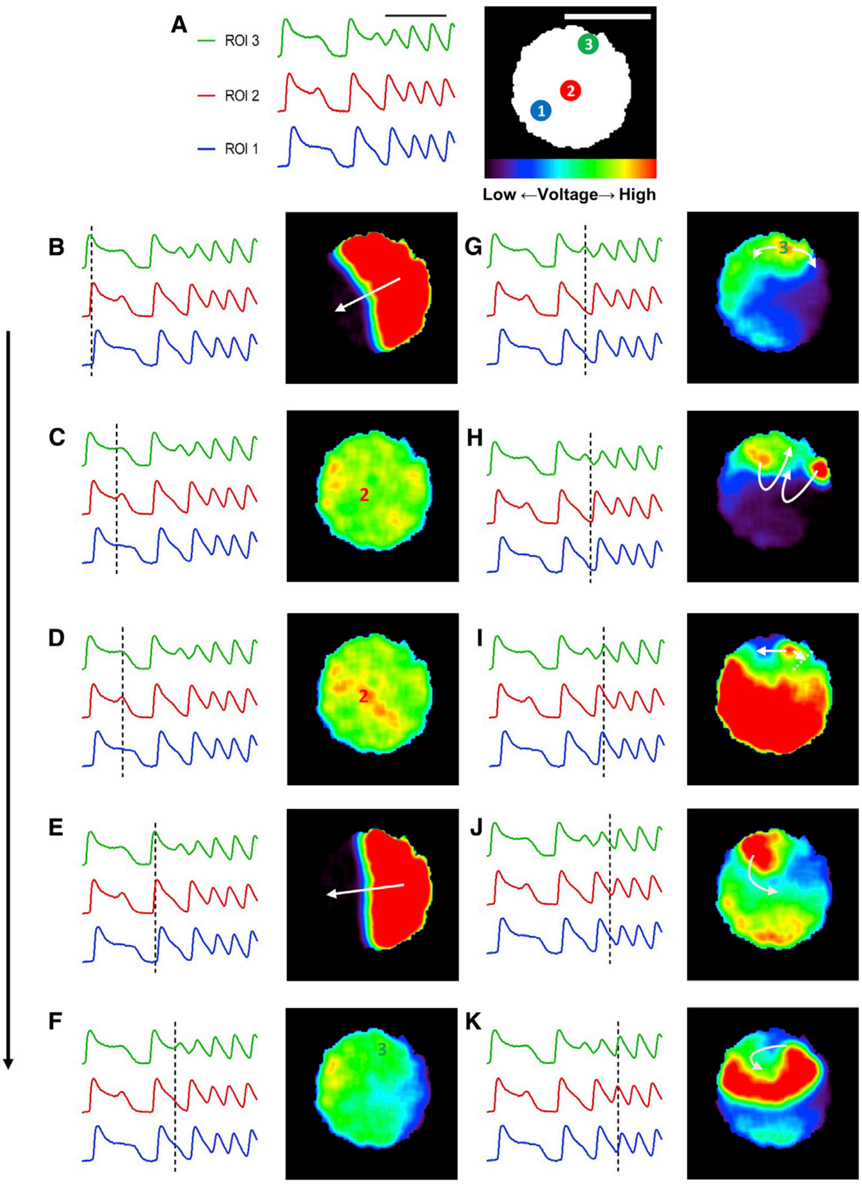

Figure 6. Fluorescence Time Lapse of Dofetilide-Induced Arrhythmogenesis

(A) Three ROIs are highlighted: (1) region with no detected triggered activity, (2) region with EAD/TA that did not develop to subsequent arrhythmia, and (3) region with TA that deteriorated into stable arrhythmia. Black scale bar: 2 s. White scale bar: 5 mm. Color scale bar represents fluorescence intensity (corresponding to voltage changes).

(B–K) Fluorescence time-lapse snapshots describing dofetilide-induced arrhythmogenesis. Note that following propagation of the first activation wave-front (B–C) and EAD/TA developed that failed to propagate and did not induce a stable arrhythmia (D). In contrast, following the second activation wave (E–F), a TA developed (G) that caused "figure-of-eight" reentry (H), unidirectional conduction block and eventually the development of a stablespiral wave (I–K).

See also Videos S6–S9.

APD prolongation at the cellular level (Leyton-Mange et al., 2014; Liang et al., 2013; Shinnawi et al., 2015; Stillitano et al., 2017; Zwi et al., 2009). Nevertheless, APD prolongation and even development of early after-depolarizations (EADs) and triggered activity (TA) are not sufficient for development of the relevant clinical arrhythmia (torsades de pointes [TdP]), which requires also the presence of an abnormal substrate at the tissue level (Antzelevitch, 2005). To study the process of drug-induced arrhythmias also at the tissue level we treated the hiPSC-CCSs with a high dose of dofetilide (50 nmol/L, Figure 6). This led to significant and diffuse APD prolongation throughout the culture, eventually causing sustained reentrant arrhythmias in five out of 12 examined hiPSC-CCSs.

By performing long-term mapping of ArcLight-hiPSC-CCSs, we were able to detect the cascade of events that

---

(F–I) Phase maps during the arrhythmia (F), during overdrive pacing (G and H), and after recovery to spontaneous normal activity (I). Black trajectories depict the meandering of the SP during each time period.

(J) Cumulative arrhythmia conversion rates in relation to rotor CL minus pacing CL (n = 7 from four independent experiments).

Scale bars: 5 mm. See also Figure S2 and Videos S4 and S5.

led to the establishment of stable dofetilide-induced arrhythmia (Video S6 and Figure 6). Notice in both the video and the resulting snapshots of the fluorescent ("potential") maps, the development of EADs/TA in localized spots (high voltage, red signal) within the hiPSC-CCS. Note that during the first activation, while APD was prolonged throughout the culture, an EAD could be detected only at one area at the center of the culture (localized increase in membrane potential [red area] at recording site 2 in Figure 6D). This EAD could not be propagated since all areas surrounding it were still relatively depolarized (homogeneous green/yellow). In the next beat, an EAD/TA developed at a different site (site 3 in Figure 6G). Due to the localized heterogeneity in the tissue, with neighboring cells already being repolarized (adjacent blue-purple areas in Figure 6G), this new ectopic activity could be propagated, generating an initial figure-of-eight reentry (Figures 6G–6I) before deteriorating into stable rotor-like activity (Figures 6I–6K).

Prevention of Dofetilide-Induced Pro-arrhythmia

To evaluate the potential role of clinically relevant treatments for TdP in our model, we tested the effects of rapid pacing and magnesium administration in preventing dofetilide-induced arrhythmias. To this end, we took advantage of the ability to study the same ArcLight-hiPSC-CCS over time and tested the incidence of arrhythmic activity following application of dofetilide alone as compared with dofetilide together with magnesium administration or rapid pacing. The electrical activity was closely monitored and resulting pro-arrhythmia was classified and scored as either non-propagating EADs/TA (Video S7, arrhythmogenic score 1), isolated propagated TA (Video S8, score 2), or stable reentrant activity (TdP, Videos S6 and S9, score 3).

Application of dofetilide resulted in significant prolongation of APD (Figures 7A and 7B) and in the generation of non-propagated EADs/TA alone in one of six cultures studied, isolated TA in two specimens, and stable reentrant activity in an additional two cultures (Figure 7D, top panel). Pacing of the dofetilide-treated hiPSC-CCSs at relatively fast rates (CL: 800–1,000 ms) shortened APD and prevented all arrhythmic events (EAD, TA, or TdP), significantly lowering the arrhythmic risk score to 0 ($p < 0.01$, $n = 6$, Figures 7D and 7E).

Co-administration of 2.1 mmol/L of $MgSO_4$ with dofetilide also prevented APD prolongation in the hiPSC-CCSs (Figures 7A and 7B, $p < 0.01$, $n = 6$). Magnesium also reduced arrhythmogenicity in the cultures with only two specimens developing dofetilide-induced EADs and none developing any propagated TA or TdP, significantly reducing the arrhythmogenicity score (Figures 7D and 7E).

DISCUSSION

The ability to derive hiPSC-CMs offers unique opportunities for cardiac regenerative medicine, disease modeling, and drug testing. In the cardiac electrophysiology field, most efforts have focused on studying the cellular properties of hiPSC-CMs, namely their AP properties and ionic current profile, with only limited studies evaluating the tissue electrical properties. However, fulfilling the unique potential of the hiPSC technology for studying more complex electrophysiological phenomena (conduction and reentry) and for evaluating long-term tissue remodeling processes and drug effects requires the development of multicellular models as well as methods for long-term, repeated, tissue phenotyping. To address these challenges, we combined hiPSC-CMs, GEVIs, and optical mapping technologies to establish a robust 2D cardiac tissue model for cardiac mapping. The established ArcLight-hiPSC-CCSs model enabled long-term and repeated phenotyping of the same cultures; detailed pharmacological studies evaluating drug effects on conduction, repolarization, and pro-arrhythmia mechanisms; and complex arrhythmia modeling focusing on the biophysical properties of rotors.

Two-dimensional rather than cellular models are important since they resemble more the native organization of cardiomyocytes within the heart and in parallel allow the induction and high-resolution mapping of tissue-related arrhythmias (Herron, 2016; Tung and Zhang, 2006). Moreover, the human origin of our cardiac cell sheets may be advantageous over the conventional animal-derived *in vitro* models such as neonatal rat ventricular myocyte cultures because of the significant interspecies differences in the expression of relevant cardiac ion channels (Wymore et al., 1997). For example, it was reported that I_{Kr} blockers could terminate spiral waves in cardiomyocyte monolayers derived from hPSCs but not from neonatal rat cardiomyocytes (Kadota et al., 2013). This difference stems from the important role of I_{Kr} in repolarization in the human, but not in the rodent, heart (Wymore et al., 1997).

The circular hiPSC-CCSs model established here follows similar efforts in the field (Herron et al., 2016; Kadota et al., 2013; Laksman et al., 2017; Lee et al., 2012) and was made possible by advancements in hPSC cardiomyocyte differentiation protocols (Burridge et al., 2014; Mummery et al., 2012), allowing the derivation of large quantities of relatively pure populations of cardiomyocytes. In this study, we generated confluent, high-density hiPSC-CCSs with high cardiomyocyte content. These characteristics are important since previous studies showed that arrhythmia inducibility was inversely correlated with cell seeding density (Kadota et al., 2013) and cardiomyocyte content (Zlochiver et al., 2008), probably because myocyte

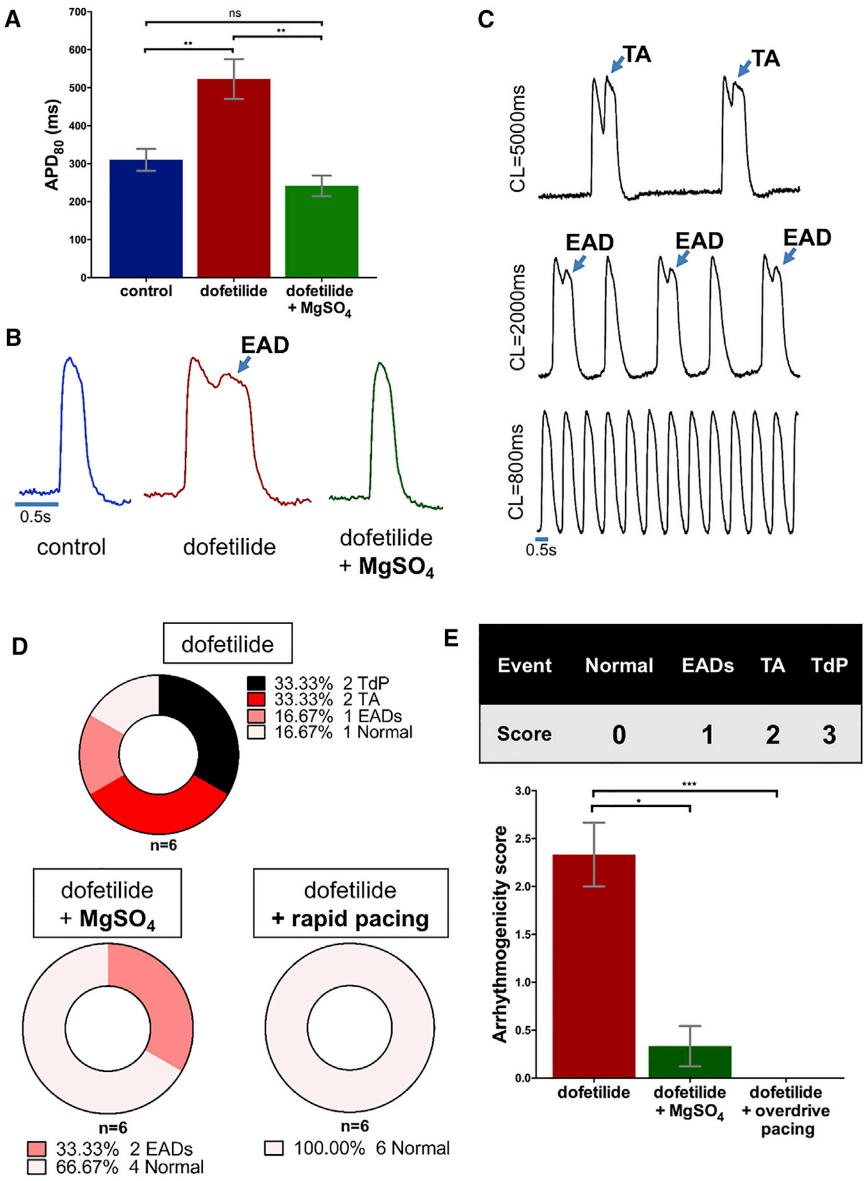

Figure 7. Prevention of Dofetilide-Induced Arrhythmogenicity by Rapid Pacing and Magnesium Sulfate

(A) Summary of dofetilide and dofetilide + $MgSO_4$ supplementation effects on APD_{80} (one-way ANOVA followed by Tukey post-hoc analysis, n = 6 from three independent experiments for each group).

(B) Representative optical APs from ArcLight-hiPSC-CCS after treatment with dofetilide or dofetilide + $MgSO_4$.

(C) Optical APs from ArcLight-hiPSC-CCS showing arrhythmogenic activity (TA and EAD) at slow pacing frequencies (CL, 5,000 and 2,000 ms) and their suppression at higher pacing frequency (CL, 800 ms).

(D) Summary of dofetilide-induced arrhythmogenicity in ArcLight-hiPSC-CCSs and its suppression by $MgSO_4$ supplementation and rapid pacing.

(E) Arrhythmogenicity scoring system and summary of $MgSO_4$ supplementation and rapid pacing on ArcLight-hiPSC-CCSs' arrhythmogenicity score (Kruskal-Wallis test followed by Dunn's multiple comparison, n = 6 from three independent experiments for each group).

Values are presented as means ± SEM. $^{*}p < 0.05$, $^{**}p < 0.01$ and $^{***}p < 0.001$. See also Videos S6–S9.

scarce areas may act as anatomical substrates for complex and fractionated conduction and reentry.

Previous reports have examined similar cell sheets by mapping of calcium transients or APs using calcium or VSDs respectively (Herron, 2016; Kadota et al., 2013; Laksman et al., 2017; Lee et al., 2012). A major limitation of using such dyes for optical mapping of cardiac cultures is their phototoxicity, which can affect cell viability and potentially alter the studied electrophysiological properties (Lopez-Izquierdo et al., 2014; Matiukas et al., 2007; Shinnawi et al., 2015), thereby significantly hampering long-term or repeated mapping. Importantly, we demonstrated that hiPSC-CCSs expressing ArcLight alone did not suffer from phototoxic effects following continuous excitation. This is opposed to sheets loaded with Di-4-ANBDQBS alone or together with ArcLight, which displayed augmented cellular damage in the illuminated centers.

One limitation of ArcLight is its relatively slow kinetics at high frequencies, leading to alterations in the fluorescent representation of phase 0 of the AP (Jin et al., 2012; Leyton-Mange et al., 2014). Since activation mapping is based on measuring LAT from the timing of phase 0 of the optical APs at each sampled pixel, this limitation could lead to inaccurate maps. When comparing the ArcLight-based optical signals with Di-4-ANBDQBS, which does not interfere with ArcLight spectrum (Matiukas et al., 2007), we could detect the typical two-stage exponential kinetics of ArcLight, characterized by an initial rapid phase that closely matches the VSD signal and a second phase where the ArcLight signal is significantly lagging behind the VSD. By targeting the initial rapid stage of phase 0 (timing of the maximal first derivative of the signal) to determine LATs, we could derive values that were almost identical between the ArcLight and VSD signals, including when using different signal-acquisition sampling rates. This allowed derivation of ArcLight-based activation and CV maps that matched those obtained by Di-4-ANBDQBS.

Based on these findings we reasoned that ArcLight-based mapping could enable reliable, long-term, and repeated phenotyping of the same specimens, allowing the study of long-term electrical remodeling processes and chronic effects of drugs or other interventions. Consequentially, by subjecting the same ArcLight-hiPSC-CCSs to repeated imaging over weeks, we identified the continuous shortening of APD over time and gradual increases in CV. To address the mechanisms underlying such CV changes, we focused on quantifying Cx43 expression (as a surrogate for changes in cellular coupling) and on Na^+ current recordings (as a surrogate for membrane excitability). Our results did not show any consistent changes in the expression of Cx43 but did reveal a significant increase in Na^+ current density over time in the hiPSC-CCSs. It is worth mentioning, however, that this increased CV is still one magnitude slower than in the native myocardium.

To demonstrate the utility of the ArcLight-hiPSC-CCS model for drug testing, we evaluated four different pharmacological agents and observed the expected dose-response effects on conduction slowing induced by suppression of gap-junction coupling (carbenoxolone) or membrane excitability (lidocaine and quinidine) and APD prolongation (dofetilide and quinidine). Moreover, the ability to use the suggested model for repeated long-term phenotyping studies can maximize the drug-screening potential, as the same specimens can be used for multiple "drug/wash" cycles to evaluate different drugs.

Importantly, while assays at the cellular level can detect APD prolongation (Caspi et al., 2009; Leyton-Mange et al., 2014; Lopez-Izquierdo et al., 2014), they lack the ability to address the degree of its heterogeneity and spatial distribution in the tissue and cannot predict drug effects on conduction. Since both CV and APD (as a surrogate for refractory period) play a role in determining the tissue wavelength (a key parameter inversely proportional to arrhythmogenic susceptibility), APD alone is not sufficient to determine the tissue's arrhythmogenic propensity.

A potential application of the hiPSC technology is in the field of safety pharmacology and specifically for "QT screening", since drug-induced APD prolongation causing life-threatening ventricular arrhythmias (TdP) is the leading cause for withdrawal of approved drugs from the market (Roden, 2004). Recent studies focused on developing screens to identify drug-induced APD prolongation using cardiomyocytes derived from human embryonic stem cells (Caspi et al., 2009; Leyton-Mange et al., 2014) or hiPSC (Liang et al., 2013; Shinnawi et al., 2015; Stillitano et al., 2017; Zwi et al., 2009). These studies, utilizing optical recordings (Lopez-Izquierdo et al., 2014) or intracellular (Liang et al., 2013) and extracellular (Caspi et al., 2009; Stillitano et al., 2017) electrophysiological measurements, primarily focused on the use of single-cell or small cell clusters and were able to detect APD prolongation and even EADs and TA. While APD prolongation, EADs, and TA are prerequisites for development of pro-arrhythmia, they are not sufficient, since development of clinical TdP requires also the presence of the necessary substrate at the tissue level (Antzelevitch, 2005).

Using continuous imaging of dofetilide-treated ArcLight-hiPSC-CCSs, we were able to map step by step the process of arrhythmia initiation and sustainment as a result of drug-induced APD prolongation ("TdP in the dish"). Our results highlight the importance of heterogeneity of repolarization in the mechanism of drug-induced arrhythmias. The development of dofetilide-induced APD prolongation and EAD/TA formation was necessary but not sufficient by itself to induce arrhythmia. The latter required, in addition, spatiotemporal repolarization heterogeneities, resulting in the presence of an already repolarized (and therefore excitable) tissue in close proximity to the site of EAD/TA formation, allowing the initiation and maintenance of complex reentrant activity.

We next demonstrated that clinically relevant interventions could prevent drug-induced arrhythmias in our model. Rapid pacing and magnesium sulfate are commonly used in the clinical management of TdP. Importantly, both treatments were also demonstrated to prevent dofetilide-induced EADs and TA and to eliminate the risk for TdP in our hiPSC-CCSs model.

In addition to drug-related arrhythmias, we were also able to induce stable spiral waves by incremental electrical stimulation protocols. These arrhythmias were then mapped and analyzed either as dynamic displays, activation maps, or by the use of phase mapping. The latter approach facilitates detailed analysis of rotor stability parameters (such as curvature and SP meandering). Since rotors may play an important role in cardiac fibrillation (Pandit and Jalife, 2013), the development of our human model may provide insights into the mechanisms of their initiation and perpetuation as well as for monitoring the effects of different therapeutic modalities. Consequentially, we were able to use our model to demonstrate the ability to interrupt and terminate rotor activity by clinically relevant interventions such as overdrive pacing and electrical cardioversion.

Among the limitations of the hiPSC-CCS model is the relatively immature state of hiPSC-CMs (Yang et al., 2014), which is an important shortcoming of the field in general. An obvious consequence is the slow CV observed within our tissues. Our measured CV values (2–7 cm/s) are in the range of some of the studies using hPSC-CM-derived tissues (Kadota et al., 2013, ~2–12 cm/s; Laksman et al., 2017, ~5.4 cm/s) but slower than values reported in others (Zhang et al., 2012, ~13–18 cm/s). This variability in CV values may stem from differences in the hPSCs lines used, in the cardiomyocyte differentiation protocols, in the culture density and cardiomyocyte content, in the culture-media used, and in the maturation stage of the hPSC-CMs. One advantage of the observed slow CV is that it leads to a shortened wavelength, which in turn can facilitate arrhythmia induction in smaller tissues, allowing down-scaling the size of the hiPSC-CCSs.

Although shown to be suitable for mapping in the current experimental conditions, the slow kinetics of ArcLight (Jin et al., 2012) may hinder perfect recapitulation of the AP morphology. This shortcoming may be solved in the future by using GEVIs with faster kinetics, such as ASAP1 (St-Pierre et al., 2014) and Arch(D95N) (Kralj et al., 2012). Lastly, our model utilizes an already established transgenic hiPSC line that expresses ArcLight constitutively (Shinnawi et al., 2015). Generating multiple stable hiPSC lines to model different disease- or patient-specific abnormalities may not be practical. This limitation may be solved by using transient lenti- or adeno-viral-based transductions of the differentiating cardiomyocytes.

In conclusion, we have established a platform for generation and mapping of 2D hiPSC-CCSs expressing a GEVI. This robust and promising platform can be widely utilized for safety pharmacology, studying arrhythmia mechanisms, and for testing various antiarrhythmic approaches.

EXPERIMENTAL PROCEDURES

Supplemental Experimental Procedures section is available online.

Cardiomyocyte Differentiation of the ArcLight-hiPSCs

We utilized a transgenic hiPSC line that stably expresses ArcLight (Shinnawi et al., 2015). Cardiomyocyte differentiation was induced using the monolayer differentiation system with a chemically defined medium supplemented with human albumin and ascorbic acid (Burridge et al., 2014).

Generation of the hiPSC-CCSs

hiPSC-CMs at d8–14 were enzymatically dissociated and seeded as circular cell sheets (~0.5 cm diameter) on Matrigel-coated culture plates (Corning) at a seeding density between 38,000 and 56,000 cells/mm^2 (0.75–1.1 million cells in 50 μL drop, Figure S1B). Tissues were cultured in RPMI/B27 containing 1% penicillin/streptomycin and blebbistatin (5 μmol/L).

Optical Mapping

The optical mapping setup consisted of a high-speed EM-CCD (electron multiplying charge coupled device) camera (Evolve 512Delta, Photometrics, 512 × 512 pixels) mounted on a fluorescent macroscope (MVX10, Olympus). Both ArcLight and Di-4-ANBDQBS containing specimens were excited using light-emitting diodes (X-Cite TURBO, Excelitas Technologies) with peak wavelengths at 475 and 630 nm, respectively. For ArcLight recordings, emission was passed through 495 nm long-pass dichroic mirror and filtered using 525/50 nm band-pass filter. A 660 nm long-pass dichroic mirror and 665 nm long-pass filter were used for Di-4-ANBDQBS recordings (all from Chroma). Fluorescence was acquired at 4 × 4 binning and a sampling interval of ~3.847 ms.

Acquisition and Analysis of Electrophysiological Parameters

OMProCCD (Huang et al., 2016), a custom-designed software, was kindly provided by Prof. Bum-Rak Choi (Brown University) and was utilized for acquisition and analysis. For generation of activation maps, LAT at each pixel was determined from the optical signals as the time point of the maximal first derivative $(dF/dt)_{max}$. APD_{80} was defined as the time interval between the LAT and the time point of 80% repolarization. Activation and APD_{80} maps were displayed as color-coded maps.

Comparison of ArcLight versus Di-4-ANBDQBS Mapping

ArcLight-hiPSC-CCSs were loaded for 7 min with RPMI/B27 medium containing 15 μg/mL (26.3 μmol/L) Di-4-ANBDQBS (purchased from Prof. Leslie Loew). Both reporters were imaged by alternating filter cubes (Figure S2A). To compare APD_{80} and MLCV values derived using the two reporters, we evaluated cultures at different developmental stages (6– 35 days) and at various pacing frequencies (CLs, 300–2,000 ms) (Figure S2A).

Drug Studies

Carbenoxolone (50 μmol/L), quinidine (0.1, 0.3, 1, 3, 10, and 30 μmol/L), lidocaine (1, 3, 10, 30, 100, and 300 μmol/L) stock solutions were dissolved in H_2O, while dofetilide (0.3, 1, 3, 10, 30, and 100 nmol/L [dose-response], 50 nmol/L [drug-induced proarrhythmia]) stock solution was dissolved in DMSO (all from Sigma-Aldrich). All recordings were performed 10 min after each dose application, except for carbenoxolone (30 min).

Electrical Stimulation and Arrhythmia Induction

A stimulus isolation unit (SIU-102, Warner Instruments) was utilized to deliver 5 ms pulses through a platinum iridium electrode (Alpha-Omega) or custom-made platinum electrodes positioned close to the tissue edge (Figures S2B and S2C). Arrhythmia inducibility was evaluated using a three-step pacing protocol: (1) incremental pacing frequency until loss of capture or induction of arrhythmia; (2) burst pacing for 3 s; and (3) direct current injection for up to 3 s.

Phase Mapping

Phase maps and related rotor biophysical parameters were computed similarly to that described previously (Gray et al., 1998; Hou et al., 2010; Iyer and Gray, 2001; Pandit and Jalife, 2013) using a semi-automated custom-written MATLAB script that generated color-coded phase maps. The SP was identified as the point where all phases of the AP conjoin (Iyer and Gray, 2001), then the meandering pathway of the SP (six steps of one rotor rotation) was calculated. Rotor radius, which is inversely proportional to the rotor's curvature, was defined as previously described (Hou et al., 2010).

Experiment Solutions

Experiments were performed at 34°C using Tyrode's solution containing (in mmol/L): NaCl, 140; KCl, 5.4; $CaCl_2$, 1.8; $MgCl_2$, 1.0; HEPES, 10; and glucose, 10 (pH 7.4 with NaOH). Prolonged experiments were performed in RPMI/B27 culture medium incubated with 95% air and 5% CO_2.

Statistical Analysis

Data are presented as mean ± SEM. Paired t test was used to compare ArcLight- and Di-4-ANBDQBS-derived SNR values and changes in mean MLCV values following carbenoxolone (50 μmol/L) administration. Repeated-measurements one-way ANOVA followed by Tukey post-hoc multiple-comparison analysis was carried out for comparison of mean MLCV and/or APD_{80} values in (1) repeated phenotyping experiments over time, (2) pharmacological dose-response experiments, and (3) the dofetilide ± $MgSO_4$ APD studies. Repeated-measurements two-way ANOVA followed by Sidak post-hoc analysis was carried out for Na^+ activation currents analysis. Kruskal-Wallis test followed by Dunn's multiple-comparison test was carried out for arrhythmogenicity score comparisons.

SUPPLEMENTAL INFORMATION

Supplemental Information includes Supplemental Experimental Procedures, five figures, and nine videos and can be found with this article online at https://doi.org/10.1016/j.stemcr.2018.04.006.

AUTHOR CONTRIBUTIONS

N. Shaheen and L.G. designed the experiments. N. Shaheen and A.S. performed the experiments, analyzed the data, and prepared the figures. I.H. and R.S. established the ArcLight hiPSC line. G.A. and A. Gepstein conducted the hiPSC cardiomyocyte differentiation. N. Setter and A. Gruber performed the western blot experiments. I.G. performed flow cytometry experiments. S.C. performed the immunostaining experiments. L.G. supervised the study. N. Shaheen, A.S., and L.G. wrote the paper.

ACKNOWLEDGMENTS

This work was supported in part by the European Research Council (ERC-2017-COG-773181-iPS-ChOp-AF), by the Technion-UHN research collaboration fund, and by the BIRAX initiative (04BX14CDLG).

Received: August 3, 2017
Revised: April 11, 2018
Accepted: April 12, 2018
Published: May 10, 2018

REFERENCES

Antzelevitch, C. (2005). Role of transmural dispersion of repolarization in the genesis of drug-induced torsades de pointes. Heart Rhythm *2*, 9–15.

Bellin, M., and Mummery, C.L. (2016). Inherited heart disease - what can we expect from the second decade of human iPS cell research? FEBS Lett. *590*, 2482–2493.

Burridge, P.W., Matsa, E., Shukla, P., Lin, Z.C., Churko, J.M., Ebert, A.D., Lan, F., Diecke, S., Huber, B., Mordwinkin, N.M., et al. (2014). Chemically defined generation of human cardiomyocytes. Nat. Methods *11*, 855–860.

Caspi, O., Itzhaki, I., Kehat, I., Gepstein, A., Arbel, G., Huber, I., Satin, J., and Gepstein, L. (2009). In vitro electrophysiological drug testing using human embryonic stem cell derived cardiomyocytes. Stem Cells Dev. *18*, 161–172.

Chen, Z., Xian, W., Bellin, M., Dorn, T., Tian, Q., Goedel, A., Dreizehnter, L., Schneider, C.M., Ward-van Oostwaard, D., Ng, J.K., et al. (2017). Subtype-specific promoter-driven action potential imaging for precise disease modelling and drug testing in hiPSC-derived cardiomyocytes. Eur. Heart J. *38*, 292–301.

Dempsey, G.T., Chaudhary, K.W., Atwater, N., Nguyen, C., Brown, B.S., McNeish, J.D., Cohen, A.E., and Kralj, J.M. (2016). Cardiotoxicity screening with simultaneous optogenetic pacing, voltage imaging and calcium imaging. J. Pharmacol. Toxicol. Methods *81*, 240–250.

Gray, R.A., Pertsov, A.M., and Jalife, J. (1998). Spatial and temporal organization during cardiac fibrillation. Nature *392*, 75–78.

Herron, T.J. (2016). Calcium and voltage mapping in hiPSC-CM monolayers. Cell Calcium *59*, 84–90.

Herron, T.J., Lee, P., and Jalife, J. (2012). Optical imaging of voltage and calcium in cardiac cells & tissues. Circ. Res. *110*, 609–623.

Herron, T.J., Rocha, A.M., Campbell, K.F., Ponce-Balbuena, D., Willis, B.C., Guerrero-Serna, G., Liu, Q., Klos, M., Musa, H., Zarzoso, M., et al. (2016). Extracellular matrix-mediated maturation of human pluripotent stem cell-derived cardiac monolayer structure and electrophysiological function. Circ. Arrhythm. Electrophysiol. *9*, e003638.

Hou, L., Deo, M., Furspan, P., Pandit, S.V., Mironov, S., Auerbach, D.S., Gong, Q., Zhou, Z., Berenfeld, O., and Jalife, J. (2010). A major role for HERG in determining frequency of reentry in neonatal rat ventricular myocyte monolayer. Circ. Res. *107*, 1503–1511.

Huang, X., Kim, T.Y., Koren, G., Choi, B.R., and Qu, Z. (2016). Spontaneous initiation of premature ventricular complexes and arrhythmias in type 2 long QT syndrome. Am. J. Physiol. Heart Circ. Physiol. *311*, H1470–H1484.

Itzhaki, I., Maizels, L., Huber, I., Zwi-Dantsis, L., Caspi, O., Winterstern, A., Feldman, O., Gepstein, A., Arbel, G., Hammerman, H., et al. (2011). Modelling the long QT syndrome with induced pluripotent stem cells. Nature *471*, 225–229.

Iyer, A.N., and Gray, R.A. (2001). An experimentalist's approach to accurate localization of phase singularities during reentry. Ann. Biomed. Eng. *29*, 47–59.

Jin, L., Han, Z., Platisa, J., Wooltorton, J.R.A., Cohen, L.B., and Pieribone, V.A. (2012). Single action potentials and subthreshold electrical events imaged in neurons with a novel fluorescent protein voltage probe. Neuron *75*, 779–785.

Kadota, S., Minami, I., Morone, N., Heuser, J.E., Agladze, K., and Nakatsuji, N. (2013). Development of a reentrant arrhythmia model in human pluripotent stem cell-derived cardiac cell sheets. Eur. Heart J. *34*, 1147–1156.

Kralj, J.M., Douglass, A.D., Hochbaum, D.R., Maclaurin, D., and Cohen, A.E. (2012). Optical recording of action potentials in mammalian neurons using a microbial rhodopsin. Nat. Methods *9*, 90–95.

Laksman, Z., Wauchop, M., Lin, E., Protze, S., Lee, J., Yang, W., Izaddoustdar, F., Shafaattalab, S., Gepstein, L., Tibbits, G.F., et al. (2017). Modeling atrial fibrillation using human embryonic stem cell-derived atrial tissue. Sci. Rep. *7*, 5268.

Lee, P., Klos, M., Bollensdorff, C., Hou, L., Ewart, P., Kamp, T.J., Zhang, J., Bizy, A., Guerrero-Serna, G., Kohl, P., et al. (2012). Simultaneous voltage and calcium mapping of genetically purified human induced pluripotent stem cell-derived cardiac myocyte monolayers. Circ. Res. *110*, 1556–1563.

Leyton-Mange, Jordan S., Mills, Robert W., Macri, Vincenzo S., Jang, Min Y., Butte, Faraz N., Ellinor, Patrick T., and Milan, David J. (2014). Rapid cellular phenotyping of human pluripotent stem cell-derived cardiomyocytes using a genetically encoded fluorescent voltage sensor. Stem Cell Reports *2*, 163–170.

Liang, P., Lan, F., Lee, A.S., Gong, T., Sanchez-Freire, V., Wang, Y., Diecke, S., Sallam, K., Knowles, J.W., Wang, P.J., et al. (2013). Drug screening using a library of human induced pluripotent stem cell-derived cardiomyocytes reveals disease-specific patterns of cardiotoxicity. Circulation *127*, 1677–1691.

Liao, M.L.C., De Boer, T.P., Mutoh, H., Raad, N., Richter, C., Wagner, E., Downie, B.R., Unsöld, B., Arooj, I., Streckfuss-Bömeke, K., et al. (2015). Sensing cardiac electrical activity with a cardiac myocyte-targeted optogenetic voltage indicator. Circ. Res. *117*, 401–412.

Lopez-Izquierdo, A., Warren, M., Riedel, M., Cho, S., Lai, S., Lux, R.L., Spitzer, K.W., Benjamin, I.J., Tristani-Firouzi, M., and Jou, C.J. (2014). A near-infrared fluorescent voltage-sensitive dye allows for moderate-throughput electrophysiological analyses of human induced pluripotent stem cell-derived cardiomyocytes. Am. J. Physiol. Heart Circ. Physiol. *307*, H1370–H1377.

Matiukas, A., Mitrea, B.G., Qin, M., Pertsov, A.M., Shvedko, A.G., Warren, M.D., Zaitsev, A.V., Wuskell, J.P., Wei, M.-d., Watras, J., et al. (2007). Near-infrared voltage-sensitive fluorescent dyes optimized for optical mapping in blood-perfused myocardium. Heart Rhythm *4*, 1441–1451.

Matsa, E., Ahrens, J.H., and Wu, J.C. (2016). Human induced pluripotent stem cells as a platform for personalized and precision cardiovascular medicine. Physiol. Rev. *96*, 1093–1126.

Moretti, A., Bellin, M., Welling, A., Jung, C.B., Lam, J.T., Bott-Flugel, L., Dorn, T., Goedel, A., Hohnke, C., Hofmann, F., et al. (2010). Patient-specific induced pluripotent stem-cell models for long-QT syndrome. N. Engl. J. Med. *363*, 1397–1409.

Mummery, C.L., Zhang, J., Ng, E.S., Elliott, D.A., Elefanty, A.G., and Kamp, T.J. (2012). Differentiation of human embryonic stem cells and induced pluripotent stem cells to cardiomyocytes: a methods overview. Circ. Res. *111*, 344–358.

Pandit, S.V., and Jalife, J. (2013). Rotors and the dynamics of cardiac fibrillation. Circ. Res. *112*, 849–862.

Roden, D.M. (2004). Drug-induced prolongation of the QT interval. N. Engl. J. Med. *350*, 1013–1022.

Shaheen, N., Shiti, A., and Gepstein, L. (2017). Pluripotent stem cell-based platforms in cardiac disease modeling and drug testing. Clin. Pharmacol. Ther. *102*, 203–208.

Shinnawi, R., Huber, I., Maizels, L., Shaheen, N., Gepstein, A., Arbel, G., Tijsen, A.J., and Gepstein, L. (2015). Monitoring human induced pluripotent stem cell-derived cardiomyocytes with genetically encoded calcium and voltage fluorescent reporters. Stem Cell Reports *5*, 582–596.

St-Pierre, F., Marshall, J.D., Yang, Y., Gong, Y., Schnitzer, M.J., and Lin, M.Z. (2014). High-fidelity optical reporting of neuronal electrical activity with an ultrafast fluorescent voltage sensor. Nat. Neurosci. *17*, 884–889.

Stillitano, F., Hansen, J., Kong, C.W., Karakikes, I., Funck-Brentano, C., Geng, L., Scott, S., Reynier, S., Wu, M., Valogne, Y., et al. (2017). Modeling susceptibility to drug-induced long QT with a panel of subject-specific induced pluripotent stem cells. eLife *6*, e19406.

Sun, N., Yazawa, M., Liu, J., Han, L., Sanchez-Freire, V., Abilez, O.J., Navarrete, E.G., Hu, S., Wang, L., Lee, A., et al. (2012). Patient-specific induced pluripotent stem cells as a model for familial dilated cardiomyopathy. Sci. Transl. Med. *4*, 130ra147.

Takahashi, K., Tanabe, K., Ohnuki, M., Narita, M., Ichisaka, T., Tomoda, K., and Yamanaka, S. (2007). Induction of pluripotent stem cells from adult human fibroblasts by defined factors. Cell *131*, 861–872.

Tung, L., and Zhang, Y. (2006). Optical imaging of arrhythmias in tissue culture. J. Electrocardiol. *39*, S2–S6.

Wymore, R.S., Gintant, G.A., Wymore, R.T., Dixon, J.E., McKinnon, D., and Cohen, I.S. (1997). Tissue and species distribution of mRNA for the IKr-like K+ channel, erg. Circ. Res. *80*, 261–268.

Yang, X., Pabon, L., and Murry, C.E. (2014). Engineering adolescence: maturation of human pluripotent stem cell-derived cardiomyocytes. Circ. Res. *114*, 511–523.

Yankelson, L., Feld, Y., Bressler-Stramer, T., Itzhaki, I., Huber, I., Gepstein, A., Aronson, D., Marom, S., and Gepstein, L. (2008). Cell therapy for modification of the myocardial electrophysiological substrate. Circulation *117*, 720–731.

Zhang, J., Klos, M., Wilson, G.F., Herman, A.M., Lian, X., Raval, K.K., Barron, M.R., Hou, L., Soerens, A.G., Yu, J., et al. (2012).

Extracellular matrix promotes highly efficient cardiac differentiation of human pluripotent stem cells: the matrix sandwich method. Circ. Res. *111*, 1125–1136.

Zlochiver, S., Muñoz, V., Vikstrom, K.L., Taffet, S.M., Berenfeld, O., and Jalife, J. (2008). Electrotonic myofibroblast-to-myocyte coupling increases propensity to reentrant arrhythmias in two-dimensional cardiac monolayers. Biophys. J. *95*, 4469–4480.

Zwi, L., Caspi, O., Arbel, G., Huber, I., Gepstein, A., Park, I.H., and Gepstein, L. (2009). Cardiomyocyte differentiation of human induced pluripotent stem cells. Circulation *120*, 1513–1523.

Stem Cell Reports, Volume *10*

Supplemental Information

Human Induced Pluripotent Stem Cell-Derived Cardiac Cell Sheets Expressing Genetically Encoded Voltage Indicator for Pharmacological and Arrhythmia Studies

Naim Shaheen, Assad Shiti, Irit Huber, Rami Shinnawi, Gil Arbel, Amira Gepstein, Noga Setter, Idit Goldfracht, Amit Gruber, Snizhanna V. Chorna, and Lior Gepstein

Supplemental Figures and Figure Legends

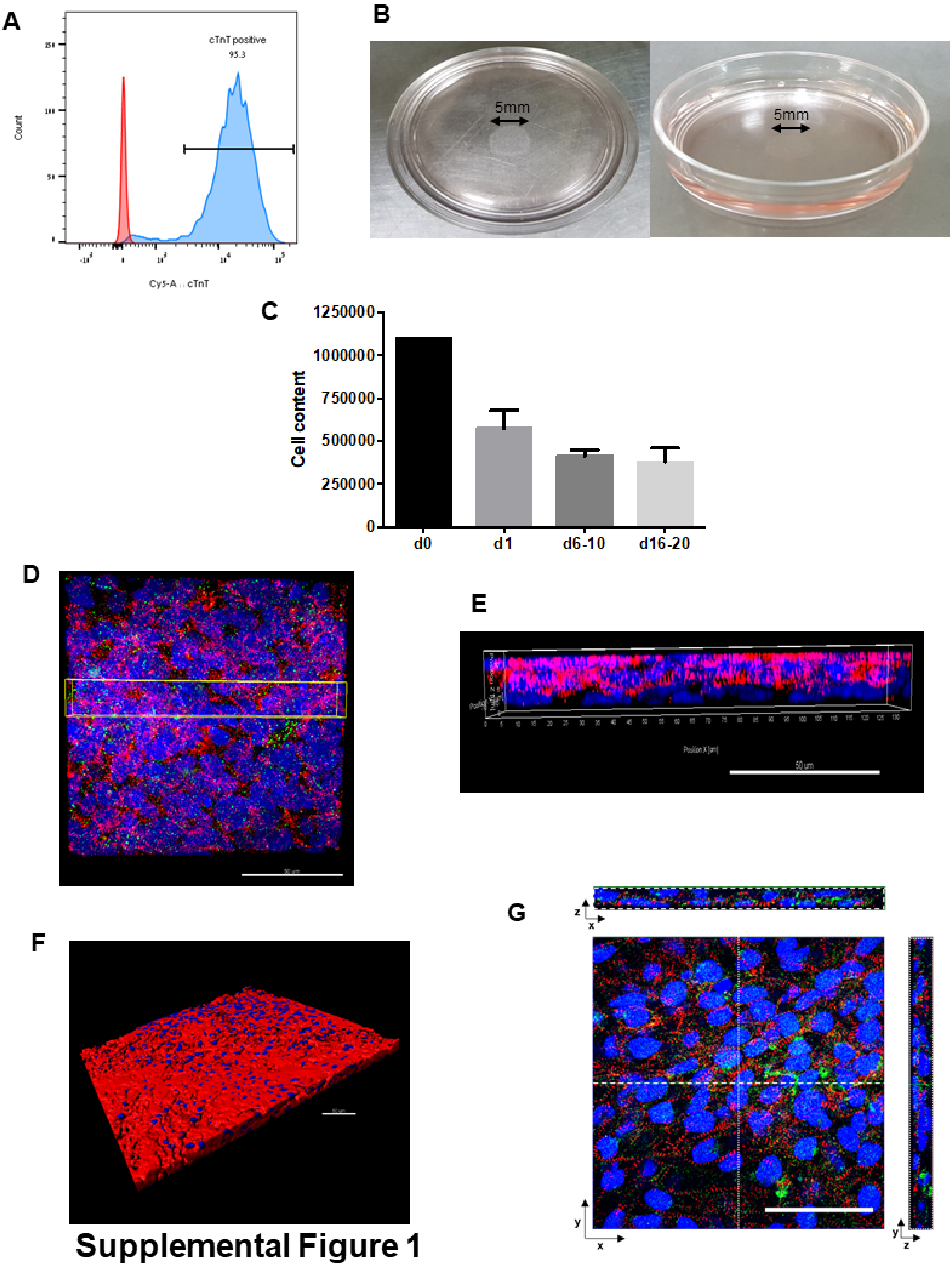

Supplemental Figure 1

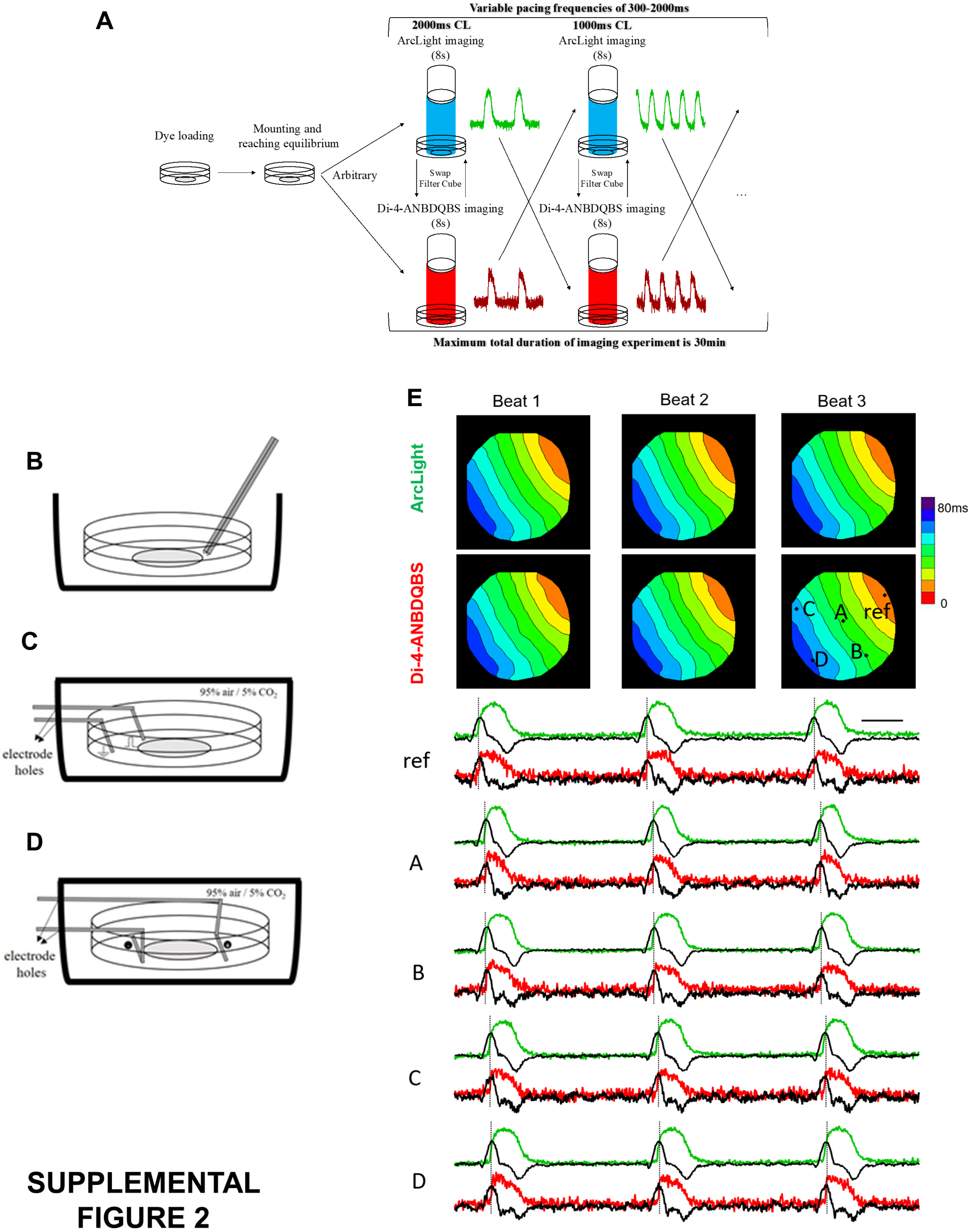

SUPPLEMENTAL FIGURE 2

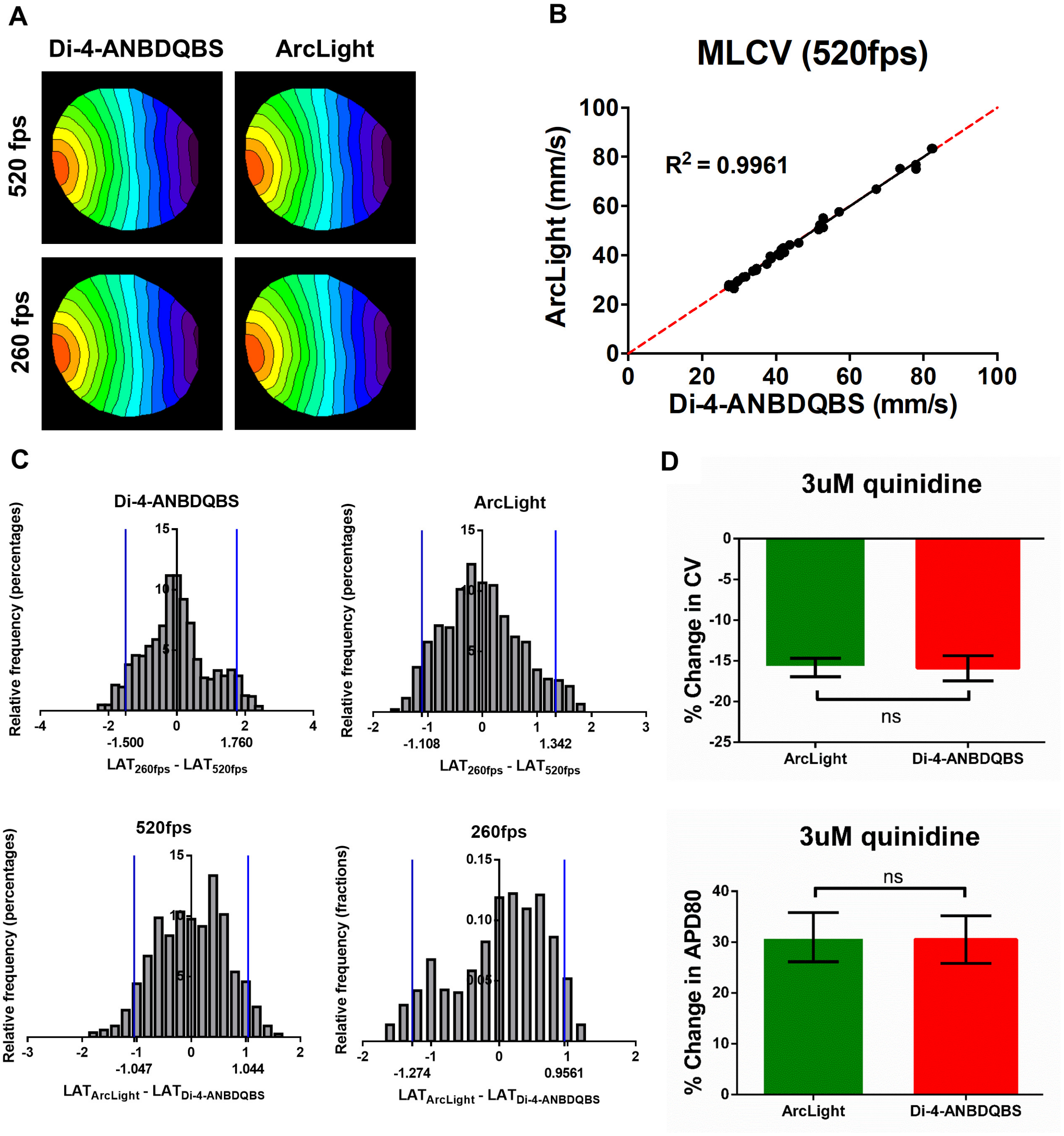

SUPPLEMENTAL FIGURE 3

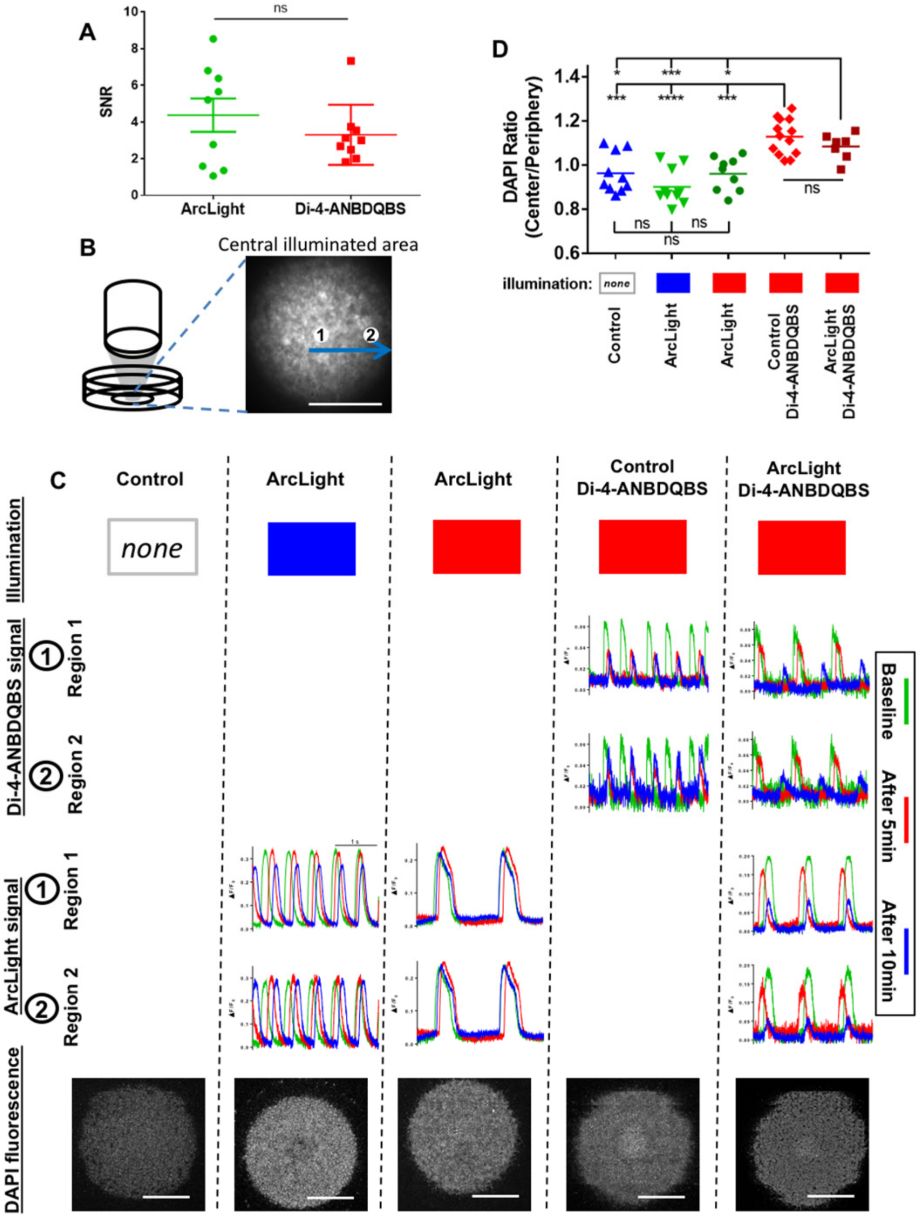

SUPPLEMENTAL FIGURE 4

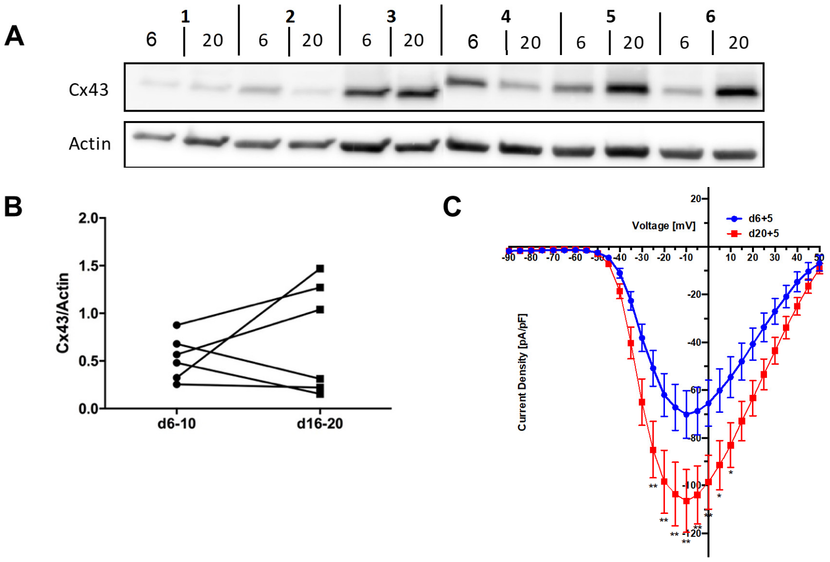

SUPPLEMENTAL FIGURE 5

Legends for Supplemental Figures

Figure S1. ArcLight-hiPSC-CCSs characterization: Flow cytometry, macroscopic view and immunostainings. Related to Figure 1. **[A]** Flow cytometry was performed to evaluate ArcLight-hiPSC differentiation efficiency using cTnT as cardiomyocyte marker (blue); red, unstained. Efficiency of >85% cardiomyocytes (cTnT+) was set as a prerequisite to generate hiPSC-cardiac cell-sheets (hiPSC-CCSs). **[B]** Macroscopic view. Due to the relative high density of seeded cells within the cardiac cell-sheets, the tissue can be visualized macroscopically. The typical approximate diameter of the seeded hiPSC-CCSs was about 5mm. **[C]** Changes in cell content per hiPSC-CCS (n=12 in 3 independent experiments) over time, with time-points of d0 (seeding point), d1, 6-10d, and 16-20d post-plating. **[D]** Top-view of 3D fluorescence stack. **[E]** Side-view of high-magnification of the yellow box from panel A. **[F]** Angle-view of 3D surface reconstruction. **[G]** Orthogonal view of fluorescence confocal planes. Dotted (right) and dashed (top) boxes show z-planes of the dotted and dashed lines, respectively. Red color represents sarcomeric α-actinin, green represents Cx43, and blue represents nuclei (DAPI). White scale-bars represent 50μm.

Figure S2. Experimental design and analysis of ArcLight and Di-4-ANBDQBS comparison. Related to Figure 1 and Experimental Procedures -Electrical stimulation and arrhythmia induction.

[A] ArcLight-hiPSC-CCSs were loaded with dye (Di-4-ANBDQBS), mounted on the heated macroscope stage to reach equilibrium and pacing electrodes were fixed. Pacing was initiated with the desired frequency, and then upon reaching steady state (at least 20 beats), the tissue culture was first imaged with one reporter's filter cube (either ArcLight or Di-4-ANBDQBS), and subsequently, the filter cube was manually swapped (using a revolver array installed on the macroscope) to the second reporter's filter cube. Delay between the two movies acquired (one for each reporter) is estimated to be less than one. **[B-D]** Pacing and incubation modes: **[B]** Bipolar pacing with top-access to tissue (incubator cover open). **[C]** Unipolar pacing with electrodes fixed (incubator cover closed). **[D]** Set-up for bi-phasic electrical cardioversion (incubator cover closed). **[E]** Arclight (green) and Di-4-ANBDQBS (red) optical AP signals. Local activation time (LAT, dashed lines) was defined as the time-point of the maxima of the AP 1st derivative (black) and resulted in similar activation maps (above two rows).

Figure S3. Reliability of ArcLight based optical mapping at high sampling interval (520) and in predicting drug response. Related to Figures 1-3

[A] Activation maps of the same ArcLight-hiPSC-CCS loaded with Di-4-ANBDQBS, generated from analysis of Di-4-ANBDQBS (left) and ArcLight (right) imaging at sampling rates of 520 (top) and 260 (bottom) frames per second (fps). **[B]** Correlation between MLCV values, as measured from ArcLight and Di-4-ANBDQBS recordings in the same cultures imaged at 520fps. Cultures from different developmental stages (6-35d) that were paced at variable rates (CLs: 300-2000ms) were used for analysis. Notice the high correlation (R^2=0.9961, n=33 in 6 independent experiments) between the two reporters. **[C]** Histogram-plots of differences in LAT values at each pixel of the activation maps shown in (A). The top-panel plots compare LAT values (LAT_{260fps}-LAT_{520fps}) derived from each reporter using different sampling rate (260 or 520fps). The bottom-panel plots compare LAT values ($LAT_{ArcLight}$-$LAT_{Di\text{-}4\text{-}ANBDQBS}$) of each sampling rate between the two reporters (ArcLight and Di-4-ANBDQBS). Vertical blue lines represent 5 and 95% percentiles. **[D]** Comparison of the change (in percent) in MLCV and APD_{80} following quinidine administration (n=5 in 3 independent experiments) as measured by Arclight (green) and Di-4-ANBDQBS (red) optical signals.

Figure S4. ArcLight versus Di-4-ANBDQBS: SNR and phototoxicity. Related to Figure 1. **[A]** SNR of ArcLight and Di-4-ANBDQBS signals obtained from the same pixels in the same hiPSC-CCSs ($P>0.05$, paired t-test, $n=9$). **[B]** Illustration (left) to indicate central illuminated area (shadowed), and high magnification of the illuminated region (right) of one ArcLight-hiPSC-CCS. Two selected ROIs are demonstrated from the central illuminated area (1 and 2). Scale bar = 1mm. **[C]** Optical signals (upper panels) obtained over 10min of continuous central illumination from two illuminated ROIs (1 and 2) and corresponding images of DAPI fluorescence intensity (lower panel) after 20min illumination and incubation with DAPI. Groups (left-to-right): non-illuminated control hiPSC-CCS, blue-illuminated ArcLight-hiPSC-CCS, red-illuminated ArcLight-hiPSC-CCS, red-illuminated Di-4-ANBDQBS loaded control hiPSC-CCS and red-illuminated Di-4-ANBDQBS loaded ArcLight-hiPSC-CCS. Note the decrease in both ArcLight and Di-4-ANBDQBS signals in the two groups loaded with Di-4-ANBDQBS. Green, red and blue colors represent optical signals acquired at baseline, 5min and 10min of illumination, respectively. Scale bar = 3mm. **[D]** Ratio of DAPI fluorescence concentration between illuminated areas and non-illuminated surroundings (one-way ANOVA followed by Tukey post-hoc analysis, $n\geq7$ for each group). **** $P<0.0001$, *** $P<0.001$, ** $P<0.01$, * $P<0.05$.

Figure S5. Evaluation of Cx43 protein content and Na^+ currents. Related to Figure 2. **[A]** Western-blot experiments of Cx43 ($n=6$). **[B]** Summary of western-blot analysis. **[C]** Comparison of Na^+ activation current density (pA/pF) between cardiomyocytes obtained from hiPSC-CCSs at day 6 (blue) and day 20 (red). ($P<0.05$, $n=13,15$, Repeated-measurements two-way ANOVA). Error bars represent SEM. *$P<0.05$, **$P<0.01$ when comparing individual current densities at the same voltage (Sidak post-hoc analysis).

Legends for Supplemental Movies

Movie S1. ArcLight versus Di-4-ANBDQBS mapping comparison. Related to Figure 1. Dynamic optical mapping displays showing action-potential propagation using ArcLight (green) or Di-4-ANBDQBS (red) fluorescence from the same ArcLight-hiPSC-CCS loaded with Di-4-ANBDQS and paced at 1 Hz.

Movie S2. Spiral-wave induction by DC current injection. Related to Figure 4 and Movie S3.
Fluorescence movie of spiral-wave (rotor) induction via DC current injection.

Movie S3. Phase-mapping of spiral-waves (rotors). Related to Figure 4 and Movie S2.
Fluorescence (upper-row) and phase (lower-row) movies of rotors induced in ArcLight-hiPSC-CCSs as acquired using the ArcLight fluorescence channel.

Movie S4. Termination of arrhythmia by electrical cardioversion. Related to Figure 5, Movies S3 and S5.
Fluorescence (left) and phase (right) movies of arrhythmia termination by 50ms field stimulation. Snapshots and analysis described in Figure 5 and in the main text.

Movie S5. Termination of arrhythmia by over-drive pacing. Related to Figure 5 and Movies S3-4.
Fluorescence (left) and phase (right) movies of arrhythmia termination by over-drive pacing. Snapshots and analysis described in Figure 5 and in the main text.

Movie S6. Dofetilide-induced arrhythmogenesis #1. Related to Figures 6-7 and Movies S7-8.
Fluorescence movie of arrhythmia induction by introduction of high dose of dofetilide (50nmol/L). Snapshots and analysis described in Figure 6 and in the main text.

Movie S7. Dofetilide-induced non-propagating EADs. Related to Figures 6-7, Movies S6 and S8-9.
Fluorescence movie showing non-propagating EADs caused by introduction of high dose of dofetilide (50nmol/L).

Movie S8. Dofetilide-induced propagating TA. Related to Figures 6-7, Movies S6-7 and S9.
Fluorescence movie showing propagating TA caused by introduction of high dose of dofetilide (50nmol/L).

Movie S9. Dofetilide-induced arrhythmogensis #2. Related to Figures 6-7 and Movies S6-8.
Fluorescence movie showing TA leading to stable arrhythmia (TdP) induction after the introduction of high dose of dofetilide (50nmol/L).

Supplemental Expanded Experimental Procedures

Maintenance of hiPSCs and cardiomyocyte differentiation

Cardiomyocyte differentiation was induced using the monolayer differentiation system (Burridge et al., 2014; Shinnawi et al., 2015). Colonies of hiPSCs were cultured on 1:200 growth factor–reduced Matrigel (Cultrex) using hESC mTeSR-1 cell culture medium (StemCell Technologies). Cells were passaged via dissociation with 0.5mM EDTA (Invitrogen) in D-PBS without $CaCl_2$ or $MgCl_2$ (Sigma-Aldrich) for 7 minutes at room temperature every 4-6 days, and replated in mTeSR medium supplemented with 2μmol/L of the ROCK inhibitor Thiazovivin (Cayman Chemicals) for the first day following passaging.

To induce differentiation, three to five days after passaging or when the cells reached 80-90% confluence (day 0 of differentiation), the culture-medium was switched to a differentiation medium CDM3 [RPMI-1640 (Gibco), recombinant human serum albumin 500μg/mL (Oryzogen), 213μg/mL, L-ascorbic acid 2-phosphate (Sigma-Aldrich), 1% penicillin/streptomycin (100 U/ml and 100 g/ml, respectively; Biological Industries)], supplemented with 6μmol/L CHIR99021 (Stemgent) for two days. On day two, medium was replaced to CDM3 medium (without CHIR) supplemented with 2μmol/L WNT-C59 (Selleckchem) for additional two days. From day 5 onwards, the cells were cultured with CDM3 medium, and medium was refreshed every other day.

On day 8-10, spontaneous contraction could be identified in the differentiating monolayers. Flow cytometry was performed routinely to ensure >85% cardiomyocyte purity by analyzing the percentage of cells that expressed cTNT (Figure S1A).

Calibration of seeding density

We aimed to obtain functional arrhythmias within our tissue cultures and to minimize the chance of anatomic reentry, thus we decided to seed the cells at maximum viable seeding densities, as it gave rise to minimum number of structural "holes". Variable approximate seeding densities were tried, and we noticed massive cell death at seeding densities higher than 56,000 cells/mm^2 as indicated by floating debris at d1 following cellular-sheet generation. Therefore, we decided to continue with seeding densities of 38,000-56,000 cells/mm^2, and discarded every hiPSC-CCS that contained microscopically-observed areas with no seeded cells ("holes").

Generation of the hiPSC-derived cardiac cellular sheets (hiPSC-CCSs)

Differentiating monolayers of hiPSC-CMs of >85% cTnT$^+$ purity at d8-14 post-differentiation were enzymatically dissociated using TrypLE 1x (ThermoFisher Sientific), passed through a 100μm strainer to obtain single-cell suspensions, and seeded as large-scale (~0.5cm diameter) circular cell-sheets on recently-dried Matrigel-coated culture-plates (Corning) at a seeding density of 38,000-56,000 cells/mm^2 (0.75-1.1 million cells in 50µl drop, Figure S1B), in RPMI/B27 (B27 supplement minus insulin, Gibco) culture medium containing 1% penicillin/streptomycin and blebbistatin [(Lee et al., 2012), 5µmol/L, Sigma-Aldrich].

We found that the factors crucial to achieve robust and efficient CCSs generation included:

(1) The use of only efficient hiPSC cardiomyocyte differentiations (resulting in >85% cTnT$^+$ differentiating cells), which is probably the most important factor; (2) The use for cell dissociations of relatively early hiPSC-CMs (before 14d of differentiation); (3) The use of single-cell suspensions following enzymatic dissociations, as we noticed that this improves the homogeneity of the generated CCSs; and (4) The use of a cell strainer (maximum 100µm). These issues were determined after a long optimization and calibration period. Only after mastering the technique and achieving robust and homogenous results in each session, did we move to perform all the experiments described in this study.

Strict adherence to this protocol yielded 80-90% successful independent-sessions, and in each successful independent-session more than 90% of the generated hiPSC-CCSs were without any structural discontinuities.

Time-dependent cell content analysis:

The generated hiPSC-CCSs were enzymatically dissociated using TrypLE 1x (ThermoFisher Sientific) and their cell content was counted using a simple hemocytometer at different time-points: d0 (seeding point), d1, d6-10, and d16-20 post-plating.

Flow cytometry

For differentiation efficiency evaluation, post-differentiation ArcLight-hiPSC-derived monolayers were routinely dissociated using TrypLE at 37°C, fixated using 4% paraformaldehyde in PBS, permeabilized with Saponin buffer (0.5% Saponin, 5% FBS in PBS) for 10min at RT, stained with primary antibody mouse anti-cardiac troponin T for 30min in 4°C (1:1000, Invitrogen, MA512960), then with secondary antibody donkey anti-mouse IgG-Cy3 for 30min at room temperature, and filtered using 40µm cell strainer before flow cytometry analysis. Analytical flow cytometry was performed using LSR Fortessa II flow cytometer (BD Biosciences), and analysis was carried out through FlowJo software.

Immunostaining studies

hiPSC-CCSs cultured on 20mm matrigel-coated glass-bottom dishes (MatTek), fixed with 4% paraformaldehyde (Bio-Lab) for 20 minutes at room temperature, washed three times in PBS, permeabilized with 1% Triton (Sigma-Aldrich) for 10min at room temperature, blocked with

5% horse serum (Gibco) for 1 hour in room temperature, and incubated overnight at 4°C with the primary antibody for sarcomeric α-actinin (1:100; mouse; Sigma-Aldrich, A7811), and for connexin-43 (1:100; Rabbit; Santa Cruz Biotechnology, sc-9059). The specimens were washed three times (each for 5 minutes) with PBS and incubated for 1 hour at room temperature in the dark with the following 1:150 diluted secondary antibody: Cy3 donkey anti-mouse IgG (715-175-150, Jackson Immunoresearch laboratories), and Cy2 donkey anti-rabbit IgG (711-225-152, Jackson Immunoresearch laboratories).

Primary and secondary antibodies were diluted in PBS containing 3% horse-serum and 0.1% Triton. Nuclei were counterstained with DAPI (1:500, Sigma-Aldrich, D9564). The preparations were examined using a Zeiss LSM-710 laser-scanning confocal microscope (Zeiss). 3D reconstruction of fluorescence z-stacks, intensity-threshold surface reconstruction, and orthogonal confocal planes were generated using Imaris software (Bitplane).

Voltage sensitive dye (VSD) loading

For experiments including comparison between ArcLight and Di-4-ANBDQBS, ArcLight-hiPSC-CCSs were loaded with fresh RPMI/B27 medium containing 15µg/ml (26.3µmol/L) Di-4-ANBDQBS (Purchased from Prof. Leslie M. Loew, U.S), at room temperature in the dark for 7min, washed twice with PBS, then the medium was switched to Tyrode’s solution for further assessment. Following experimental procedures, Di-4-ANBDQBS loaded cellular-sheets were discarded, and were not used for further experimentation.

Optical mapping

The optical mapping setup consisted of a high speed EMCCD camera (Evolve® 512 Delta, Photometrics, 512x512 pixels) mounted on a fluorescent macroscope (MVX10, Olympus) equipped with 0.25 NA 6.3X - 63X (MVPLAPO 1X, Olympus, used for almost all experiments) and 0.5 NA 12.5X - 125X (MVPLAPO 2XC, Olympus, used only for DAPI viability assay, see below Evaluation of phototoxicity) objectives. The default field of view (FOV) achieved for illumination and imaging by using the 1X objective and setting the zoom body on 2.5X was 10mm. However, for focused central excitation in the phototoxicity experiments, the 2X objective and 6.3X in the zoom body were used to achieve ~2mm FOV. Both ArcLight and Di-4-ANBDQBS containing specimens were excited using LEDs (X-Cite® TURBO, Excelitas Technologies) with peak wavelengths at 475 and 630 nm, respectively. For ArcLight recordings, emission was passed through 495 long-pass dichroic mirror and filtered using 525/50 band-pass filter. While a 660 long-pass dichroic mirror and 665 long-pass filter were used for Di-4-ANBDQBS recordings (All from Chroma). Fluorescence was acquired at 4x4 binning, and a sampling interval of 3.847ms (~260 frames per second) at all experiments. To compare mapping results at different sampling rates we acquired the data for both ArcLight and Di-4-ANBDQBS also at a sampling interval of ~1.923ms (520 frames per second, 8x8 binning).

ArcLight vs. Di-4-ANBDQBS mapping comparison

ArcLight-hiPSC-CCSs were loaded with Di-4-ANBDQBS and both reporters were imaged by alternating filter cubes using the optical mapping setup as described above. To compare the accuracy of the electrophysiological parameters (APD_{80} and MLCV values) derived using the two reporters, we evaluated cultures at different developmental stages (6-35d) and at various pacing frequencies (CLs: 300-2000ms) (Figure S2A). Pacing was initiated with the desired frequency, and then upon reaching steady state (at least 20 beats), the tissue culture was first imaged with one reporter's filter cube (either ArcLight or Di-4-ANBDQBS), and subsequently, the filter cube was manually swapped (using a revolver array installed on the macroscope) to the second reporter's filter cube. Delay between the two movies acquired (one for each reporter) was estimated to be less than one second.

Evaluation of signal-to-noise ratio (SNR)

To compare SNR for ArcLight and Di-4-ANBDQBS imaging, we first performed a series of preliminary studies to determine the optimal loading conditions (concentration and incubation time) of Di-4-ANBDQBS. This calibration results in optimal loading conditions of 60µg/mL for 20min at room temperature. Next, from each 8 seconds recording of ArcLight-hiPSC-CCSs loaded with Di-4-ANBDQBS and paced at 1Hz, we sampled one random pixel for analysis. Fluorescence signal was inverted and normalized (transformed to $\Delta F/F_{min}$) for further analyses. For each AP, $(\Delta F/F)_{baseline}$ was calculated as the average of 50ms diastolic segment (100ms to 50ms prior to AP activation time) and the amplitude was defined as $(\Delta F/F)_{peak}$-$(\Delta F/F)_{baseline}$. SNR was defined as the amplitude divided by the root-mean-square of the baseline segment (SNR_A, Figure S4A). Likewise, SNR was calculated using four additional formulas based on the derived ΔF/F signal (SNR_{B-E}, data not shown)

$$SNR_A = \frac{Amp}{RMS_{baseline}};\ SNR_B = \frac{Amp}{SD_{baseline}};\ SNR_C = \frac{Amp}{\sqrt{\frac{VAR_{baseline}}{n}}};$$

$$SNR_D = \frac{RMS_{peak} - RMS_{baseline}}{RMS_{baseline}};\ SNR_E = \frac{RMS_{peak}}{RMS_{baseline}}$$

RMS = root mean square; SD = standard deviation; VAR = variance. Baseline = 50ms diastolic segment (100ms to 50ms prior to activation time); Amp: peak value minus baseline mean; n = number of frames of the baseline segment (in our case: 26).

Evaluation of phototoxicity

The central portion (2mm diameter) of the hiPSC-CCSs was continuously illuminated with blue- (475nm, 12mW, “ArcLight alone” hiPSC-CCSs) **<u>or</u>** red- (670nm, 12mW, "ArcLight alone", "ArcLight + Di-4-ANBDQBS" and "Di-4-ANBDQBS alone") excitation lights for 20 min. hiPSC-CCSs not expressing either reporters nor illuminated were used as a control group [used from the original hiPSC-cell line prior to the transgenic introduction of Arclight (Shinnawi et al., 2015)]. In some of the cultures, we also performed optical recordings at baseline and at 5 and 10 minutes following the initiation of illumination. At the end of the illumination period, the specimens from all five groups were incubated with 1:500 DAPI (Sigma-Aldrich) in PBS at room temperature for 3 minutes, washed with PBS and imaged with Zeiss LSM-710 laser-scanning confocal microscope. DAPI concentration (fluorescence intensity normalized per area) ratio between central (illuminated) and peripheral (non-illuminated) regions was calculated for each hiPSC-CCS ("DAPI center/periphery ratio"). DAPI emission was collected by whole hiPSC-CCS scanning using 5x5 array of 1024x1024 pixel frames to give 6x6mm full frames. In addition, DAPI concentration (fluorescence intensity normalized per area) ratio between central (illuminated) and peripheral (non-illuminated) regions was calculated for each hiPSC-CCS (DAPI center/periphery ratio).

Acquisition and analysis of electrophysiological parameters

<u>Platform for signal processing and data analysis</u>: Micro-Manager was used for acquisition in the SNR, phototoxicity and acquisition speed comparison experiments. For all other experiments, OMProCCD (Huang et al., 2016; Kim et al., 2015), a custom-designed software based on Interactive Data Language (IDL 8.5; Exelis Visual Information Solutions, received as a generous gift from Prof. Bum-Rak Choi, Brown University) was utilized for acquisition and analysis.

<u>Excluding bad pixels</u>: bad pixels were discarded by both threshold-based automatic and manual exclusion; only relevant pixels, which resembled tissue-filled area, were analyzed.

<u>Filtration</u>: data was filtered using spatial smooth filter (3x3 pixels), then, using polynomial temporal filter (3rd order, 13 points window size). Similarly, polynomial temporal filter was also applied on the first derivative dF/dt (3rd order, 30 points window size).

<u>Calculation of local activation time (LAT), APD_{80}, conduction velocity (CV) and their related maps</u>: LAT for each electrical wave at a specific pixel was determined as the time-point of maximal 1st derivative $(dF/dt)_{max}$. Local APD_{80} was used as a surrogate for APD (Herron, 2016; Hou et al., 2010; Muñoz et al., 2007) and was determined as the time interval between LAT and time-point of 80% repolarization of the optical action potential. Local CV vector was calculated as the distance of action potential propagation over time-intervals calculated from LATs of 5x5 square of pixels and assigned to the central relevant pixel. Activation, APD_{80} and CV maps were subsequently generated by plotting colored local activation time values, local APD_{80} values and local CV values of all relevant pixels per beat. Averaged maps

for the same parameters were generated for each recording by averaging at least 4 beats. Mean local CV (MLCV), and mean APD_{80} were calculated as the mean of all relevant pixel values per recording.

Pharmacological studies and solutions

For single-dose experiments (carbenoxolone), recordings were performed in Tyrode's solution at 30 minutes post drug administration. For all other drug studies, long (1>hour) dose-response experiments were performed while maintaining hiPSC-CCSs in fresh culture medium (RPMI/B27) and incubated in 95% air, 5% CO_2 (200ml/minute). Recordings were acquired 10 minutes after the administration of each dose. Tyrode's solution contained (in mmol/L): NaCl-140, KCl-5.4, $CaCl_2$-1.8, $MgCl_2$-1.0, HEPES-10 and glucose-10 (pH-7.4 with NaOH). Carbenoxolone (working concentration: 50μmol/L), quinidine (0.1, 0.3, 1, 3, 10 and 30μmol/L) and lidocaine (1, 3, 10, 30, 100 and 300μmol/L) stock solutions were dissolved in H_2O, while dofetilide (0.3, 0.3, 1, 3, 10, 30 and 100nM) stock solution was dissolved in DMSO. All drugs were purchased from Sigma-Aldrich.

Electrical stimulation and arrhythmia induction

A stimulus isolation unit (SIU-102, Warner-instruments) was utilized to deliver 5ms pulses through a platinum iridium electrode (Alpha-Omega, Figure S2B) or custom-made platinum electrodes positioned close to the tissue edge (Figure S2C) at varying pacing frequencies (300-2000ms cycle-lengths [CLs] for MLCV and APD comparison between ArcLight and Di-4-ANBDQBS. 1000, 800, 600 and 500ms CLs to derive restitution curves). Arrhythmia inducibility was evaluated using a three-step-pacing protocol: (1) Incremental pacing frequency (CLs-1000, 800, 600, 500, 400, 300, 250, 200ms) until loss of capture or induction of arrhythmia (maximum stimulation current intensity was set to 3x of 1 Hz 100% capture threshold); (2) Burst pacing (20ms intervals, 5ms stimulus duration, 3x threshold) for 3s; and if arrhythmia was not initiated (3) DC current injection for up to 3s (3x threshold).

Phase mapping

Phase-maps and related rotor biophysical parameters were computed similarly to that described previously (Gray et al., 1998; Iyer and Gray, 2001; Pandit and Jalife, 2013) using a semi-automated custom-written MatLab script. The code contains an algorithm, which loads a fluorescence-images stack of at least two rotor rotations as an input, and plots the fluorescence of each pixel versus the fluorescence of the same pixel in a consecutive frame within an approximate interval of $0.25APD_{80}$.

The phase at a certain time-point for each pixel is derived as the rotation angle (in radians, between $-\boldsymbol{\pi}$ and $\boldsymbol{\pi}$) observed in the plot of the two fluorescence values around the mean. This allows the generation of two-dimensional color-coded phase maps representing the phase values at each pixel. Singularity points (SPs) were identified as the points where all phases conjoin (Iyer and Gray, 2001). Meandering pathway of the SP was calculated as the sum of distances that the SP moves in 6 steps of one rotor rotation. Wave-front and wave-tail were defined as two continuous lines, which connect pixels having phase values between -1.85 and -1.75 rad (for wave-front), and between 3.1 and 3.14 rad (for wave-tail). Rotor radius, which is inversely-proportional to curvature, was obtained as previously described (Hou et al., 2010; Muñoz et al., 2007). From a representative snapshot of the phase stack, the tangent of the SP was computed by linear regression of the wave-front pixel locations in the immediate vicinity of the SP (closest 6-15 identified pixels of wave-front including the singularity point), and a perpendicular line was extended from the SP to cross the wave-front. The length of the perpendicular line was defined as rotor radius.

Dofetilide-induced arrhythmia, rapid pacing and $MgSO_4$ arrhythmia prevention experiments

High dose dofetilide (50nmol/L) was administered either alone or in combination with 2.1mmol/L $MgSO_4$. hiPSC-CCS were continuously paced at 0.2Hz throughout the experiment. For rapid pacing experiments, hiPSC-CCSs treated with dofetilide (50nmol/L) and pacing at 1-1.25Hz (1000-800s CL). The electrical activity in the cultures was closely monitored and the resulting arrhythmogenicity was classified and scored as either the development of non-propagating EADs (Movie S7, arrhythmogenic score-1), isolated propagated TA (Movie S8, score-2), or the development of stable re-entrant activity (Movies S6 and S9, TdP, score-3).

Western-blot

hiPSC-CCS on days 6 and 20 post plating were lysed with ice-cold RIPA lysis buffer and protease inhibitor (Sigma). 40µg of protein from the samples were mixed and resolved in 4x Laemmli Sample Buffer (BioRad) and incubated in 37°C for 40 minutes before loading on polyacrylamide gels (Bio-Rad). The electrophoresed proteins were transferred to PVDF membranes (Bio-Rad). The membranes were incubated for 60 minutes with 3.5% dry milk (Santa Cruz) and Tris-buffered saline (TBST) to block nonspecific binding sites. The specific primary antibodies used for detection of antigens of interest: anti Nav1.5 (1:400 in 5% BSA in TBST, alomone ASC-013), anti α-actinin (1:2500 in 3.5% milk in TBST, sigma A7811), anti Cx43 (1:500 in 5% BSA in TBST, Santa Cruz sc-9059), anti β-actin (1:1000 in 3.5% milk in TBST, Abcam 8224). The membrane was incubated with the primary antibodies overnight at 4°C and secondary antibodies for 2h at room-temperature (BioRad, 1:5000 in 3.5% milk in TBST). Primary antibody incubation followed by HRP-coupled secondary antibodies

(BioRad). Proteins were revealed with ECL Prime (BioRad) and images were acquired using a LAS4000 Camera (GE Healthcare). For quantitation, band intensities were measured using ImageJ.

Sodium currents measurements

Paired (generated at the same dependent-session) hiPSC-CCSs on days 6 and 20 post plating were enzymatically dissociated and re-plated as single cells on Matrigel-coated glass bottom dishes (MatTek). Sodium currents (I_{Na}) were recorded 5 days post plating from single hiPSC-CMs using the whole-cell patch clamp technique at voltage-clamp mode. Data was amplified, acquired and analyzed using MultiClamp 700B, Digidata 1440A and pClamp10, respectively. Whole-cell capacitance along with series resistance compensation (≥75%) was applied and I_{Na} currents were elicited by applying 50ms depolarizing steps from a holding potential of -90mV to voltages between -90 and 50mV in 5mV increments. Experiments were performed at room temperature with extra-cellular solution consisting of (in mmol/L): NaCl-140, CsCl-5.4, $CaCl_2$-1.8, $MgCl_2$-1, glucose-10, HEPES-10, and nifedipine-0.01 (pH-7.4 with CsOH) while the pipette solution consisted of (in mmol/L): NaCl-3, CsCl-133, $MgCl_2$-2, Na_2ATP-2, TEA-CL-2, EGTA-10, HEPES-10, (pH-7.3 with CsOH). Data was digitized at 20 KHz and filtered using 5 KHz low-pass filter.

Statistical analysis

Data is presented as mean±SEM. Paired t-test was used to compare ArcLight- and Di-4-ANBDQBS- derived MLCV, APD_{80} and SNR values as well as changes in mean MLCV and APD_{80} values following carbenoxolone (50µmol/L) and quinidine (3µmol/L) administration. Repeated-measurements one-way ANOVA followed by Tukey post-hoc multiple-comparison analysis was carried out for comparison of mean MLCV and APD_{80} values in: (1) repeated-phenotyping experiments over time, (2) in pharmacological dose-response experiments and (3) in the dofetilide±$MgSO_4$ APD studies. Similalry, Repeated-measurements one-way ANOVA followed by Tukey post-hoc multiple-comparison analysis was carried out for DAPI ratio comparisons. Repeated-measurements two-way ANOVA followed by Sidak post-hoc analysis was carried out for Na^+ activation currents analysis. Kruskal-Wallis test followed by Dunn's multiple comparison test was carried out for arrhythmogenicity score comparisons.

Supplemental References

Burridge, P.W., Matsa, E., Shukla, P., Lin, Z.C., Churko, J.M., Ebert, A.D., Lan, F., Diecke, S., Huber, B., Mordwinkin, N.M.*, et al.* (2014). Chemically defined generation of human cardiomyocytes. Nat Methods *11*, 855-860.

Gray, R.A., Pertsov, A.M., and Jalife, J. (1998). Spatial and temporal organization during cardiac fibrillation. Nature *392*, 75-78.

Herron, T.J. (2016). Calcium and voltage mapping in hiPSC-CM monolayers. Cell Calcium *59*, 84-90.

Hou, L., Deo, M., Furspan, P., Pandit, S.V., Mironov, S., Auerbach, D.S., Gong, Q., Zhou, Z., Berenfeld, O., and Jalife, J. (2010). A major role for HERG in determining frequency of reentry in neonatal rat ventricular myocyte monolayer. Circ Res *107*, 1503-1511.

Huang, X., Kim, T.Y., Koren, G., Choi, B.-R., and Qu, Z. (2016). Spontaneous initiation of premature ventricular complexes and arrhythmias in type 2 long QT syndrome. Am J Physiol Heart Circ Physiol *311*, H1470-H1484.

Iyer, A.N., and Gray, R.A. (2001). Experimentalist's approach to accurate localization of phase singularities during reentry. Ann Biomed Eng *29*, 47-59.

Kim, T.Y., Kunitomo, Y., Pfeiffer, Z., Patel, D., Hwang, J., Harrison, K., Patel, B., Jeng, P., Ziv, O., Lu, Y.*, et al.* (2015). Complex excitation dynamics underlie polymorphic ventricular tachycardia in a transgenic rabbit model of long QT syndrome type 1. Heart Rhythm *12*, 220-228.

Lee, P., Klos, M., Bollensdorff, C., Hou, L., Ewart, P., Kamp, T.J., Zhang, J., Bizy, A., Guerrero-Serna, G., Kohl, P.*, et al.* (2012). Simultaneous voltage and calcium mapping of genetically purified human induced pluripotent stem cell-derived cardiac myocyte monolayers. Circ Res *110*, 1556-1563.

Muñoz, V., Grzeda, K.R., Desplantez, T., Pandit, S.V., Mironov, S., Taffet, S.M., Rohr, S., Kléber, A.G., and Jalife, J. (2007). Adenoviral expression of IKs contributes to wavebreak and fibrillatory conduction in neonatal rat ventricular cardiomyocyte monolayers. Circ Res *101*, 475-483.

Pandit, S.V., and Jalife, J. (2013). Rotors and the dynamics of cardiac fibrillation. Circ Res *112*, 849-862.

Shinnawi, R., Huber, I., Maizels, L., Shaheen, N., Gepstein, A., Arbel, G., Tijsen, A.J., and Gepstein, L. (2015). Monitoring human induced pluripotent stem cell-derived cardiomyocytes with genetically encoded calcium and voltage fluorescent reporters. Stem Cell Rep *5*, 582-596.